X-ray imaging and analysis techniques for quantifying pore-scale structure and processes in subsurface porous medium systems

Dorthe Wildenschild [a,*], Adrian P. Sheppard [b]

[a] School of Chemical, Biological, and Environmental Engineering, Oregon State University, Corvallis, OR 97331, USA
[b] Department of Applied Mathematics, Research School of Physics and Engineering, Australian National University, Canberra, ACT 0200, Australia

A R T I C L E   I N F O

A B S T R A C T

We report here on recent developments and advances in pore-scale X-ray tomographic imaging of subsurface porous media. Our particular focus is on immiscible multi-phase fluid flow, i.e., the displacement of one immiscible fluid by another inside a porous material, which is of central importance to many natural and engineered processes. Multiphase flow and displacement can pose a rather difficult problem, both because the underlying physics is complex, and also because standard laboratory investigation reveals little about the mechanisms that control micro-scale processes. X-ray microtomographic imaging is a non-destructive technique for quantifying these processes in three dimensions within individual pores, and as we report here, with rapidly increasing spatial and temporal resolution.

1. Introduction

Understanding porous media flow and transport, and in particular multi-phase flow, is of central importance to many natural and engineered processes; groundwater and vadose zone flow and transport, contaminant remediation, oil recovery processes, and energy-related activities such as geothermal energy production, and geologic sequestration of CO_2.

We provide here an overview of recent advances and developments in the application of X-ray microtomography to subsurface flow and transport problems, with a particular emphasis on multi-phase flow. Why tomography? Because it is the one non-destructive technique that will reliably produce information, in three dimensions and for opaque porous media, about processes and variables of importance to subsurface flow and transport phenomena. New methods such as FIB-SEM (focused ion beam-scanning electron microscopy) and TEM (transmission electron microscopy) tomography are also rapidly developing, but operate at a scale that is not well-suited for exploration at a representative elementary volume (REV) scale that is relevant for fluid flow and transport. Thus, this review is focused on processes taking place at the micro-scale – also referred to here as the pore-scale, i.e., the scale at which individual grains and fluid interfaces can be resolved and identified. It is the scale at which many physical and chemical phenomena are rooted, and it has been shown repeatedly that larger-scale processes are often governed by these small-scale phenomena. Simultaneously, we have focused our effort away from nano-scale characterization, mainly because we are interested in linking micro-scale processes with continuum-scale properties, and therefore need to consider sample volumes that are large enough to be representative of the material as a whole. Our pore-scale focus means that we neglect a vast body of research at both larger and smaller scales, and yet we recognize that today's understanding of these processes is founded on the work that has addressed – and continues to address – both nano-scale and continuum-scale processes. We have also chosen not to cover the vast field of pore-scale numerical modeling that is often a natural extension of high-resolution imaging, mainly because a thorough review of the literature would warrant a separate manuscript.

The overall goal of this review article is to provide an overview of current state-of-the-art in tomographic imaging using both synchrotron and laboratory-scale facilities, utilizing both polychromatic and monochromatic radiation. Our aim is to provide a comprehensive review of possible applications of the technique in the fields of water resources, hydrology, petroleum engineering, environmental engineering, soil science, and energy exploration and waste storage, to stimulate future use of the technique, and foster continued development as the user communities grow. In Section 2, we provide an overview of the three tomography techniques included in this review, transmission (or absorption contrast, by far the most common), phase contrast, and fluorescence. In Section 3, we introduce the different X-ray sources and give an overview of how these capabilities have evolved over time, introduce reconstruction methods, and discuss future trends. Different process-based experimental techniques are covered in Section 4, while Section 5 addresses analysis and quantification

* Corresponding author.
E-mail addresses: dorthe@engr.orst.edu (D. Wildenschild), adrian.sheppard@anu.edu.au (A.P. Sheppard).

of the commonly large datasets acquired. Finally, Section 6 is a comprehensive overview of a wide range of applications of these imaging techniques to subsurface processes which have been imaged/studied at the pore-scale, and using quantitative methods.

Different terminology is often being used by different groups working with X-ray microtomographic imaging (micro-CT, CMT, XMT, etc.), however, we will use the term MCT in the remainder of this article to refer to the technique.

2. Imaging techniques

Because our focus is on *imaging* techniques, this review only discusses transmission, phase, and fluorescence tomography.

2.1. Transmission X-ray microtomography

2.1.1. Theory

When photons interact with solids and complex biological materials they are absorbed, scattered (elastic or inelastic), diffracted, refracted, or transmitted through the material. During absorption of photons, emission of electrons, visible light, and X-rays also takes place. At its most basic level, absorption of X-rays occur when an incoming X-ray photon is absorbed, and this results in the ejection of electrons from the inner shell of the atom, and the atom is ionized. The ionized atom will eventually return to its neutral state (filling the vacated spot in the inner shell) often with the emission of an X-ray characteristic of the atom. As they pass through a solid object, the attenuation of X-rays follows Lambert–Beer's law:

$$I = I_0 \exp(-\mu x) \tag{1}$$

where I is the attenuated intensity after the X-rays have passed through an object of thickness x, I_0 is the incident radiation intensity, and μ is the linear attenuation coefficient.

The Lambert–Beer law is strictly only valid for a pure monochromatic beam, i.e. one in which all photons have the same energy and wavelength. All current X-ray sources (with the exception of the free electron laser, see Section 3.2) produce polychromatic beams, which are the analogue of white light in being composed of a spectrum of photon energies. Therefore, unless a monochromator has been used to discard all but a few selected energies (see Section 2.1.3), the light will be composed of a plurality of energies. Since the attenuation coefficient μ varies with energy, the beam intensity does not decay exponentially (see Section 2.1.2). The attenuation coefficient also depends on the atomic electron density and the bulk density of the material. For low X-ray energies (50–100 keV), photoelectric absorption (which is strongly dependent on atomic number) dominates X-ray interaction with matter. However, for higher energies, up to 5–10 MeV, photon attenuation is mainly caused by Compton scatter, and is therefore largely controlled by electron density. Finally, for photon energies beyond 10 MeV, interaction is dominated by pair production, e.g. [14]. A more detailed description of X-ray attenuation and its relative dependence on these various components as a function of X-ray energy can be found in e.g. [14,15]. From Eq. (1) we see that I is a decreasing function of distance, x, (the exponential argument is negative), indicating that the incident X-rays, I_0, are attenuated as they pass through the object. Materials with a high attenuation coefficient will therefore allow X-rays to penetrate only a relatively short distance, whereas materials with a low attenuation coefficient are more easily penetrated. Absorption properties of both elements and compounds for a wide range of energies can be accessed via various on-line resources, for instance the NIST XCOM Photon Cross-sections Database (http://www.nist.gov/pml/data/xcom/index.cfm).

From Eq. (1) it is seen that if the incident intensity, I_0, as well as $I(x)$ can be measured, it is possible to calculate the average linear attenuation coefficient of the (composite) material. Because attenuation coefficients for composite materials add linearly, and if the volume fractions, X_v are known, it is straightforward to also compute linear attenuation coefficients for the composite parts. To accurately identify/classify objects or materials of different composition and density accurately, we therefore need sufficient variation in attenuation coefficients. To acquire data in three dimensions, the object is rotated in the beam and a large number of two-dimensional radiographic projections are collected at different angles such that the full three-dimensional distribution of attenuation coefficients can be mathematically back-calculated, i.e., reconstructed as described in Section 3.4.

2.1.2. Beam hardening correction

As discussed above, all sources of X-rays currently used in MCT generate a polychromatic beam, i.e. one that contains a spectrum of X-ray energies and wavelengths. In general, for a given material, the attenuation coefficient decreases with photon energy, i.e. more energetic ("harder") beams have more penetrating power. As a polychromatic beam passes through an attenuating material, the lower energies (softer X-rays) are absorbed more, resulting in a beam spectrum relatively depleted in lower energies. The beam is said to have become harder, and this harder beam is then attenuated less as it continues further into the material. The beam sees a higher effective attenuation coefficient at the beginning of its passage through a material than further in. If tomographic image reconstruction is performed using the Lambert–Beer law this will cause an object of uniform material to appear more attenuating near its edges. Fig. 1 shows an example of this so-called beam hardening artifact.

This is a severe problem for medical scanners which have shipped with some form of beam hardening correction since the early 1980s, usually based on the method introduced by Herman in 1979 [16]. The artifact, even when minor, is an insidious problem for downstream analysis since it represents a large-scale, gradual inhomogeneity. It is for this reason that monochromators are ubiquitous at synchrotron beamlines, where one can afford to reject the bulk of the beam flux. Unfortunately, there is no perfect method for correcting the beam hardening artifact for anything but single-material objects, since different elements harden the
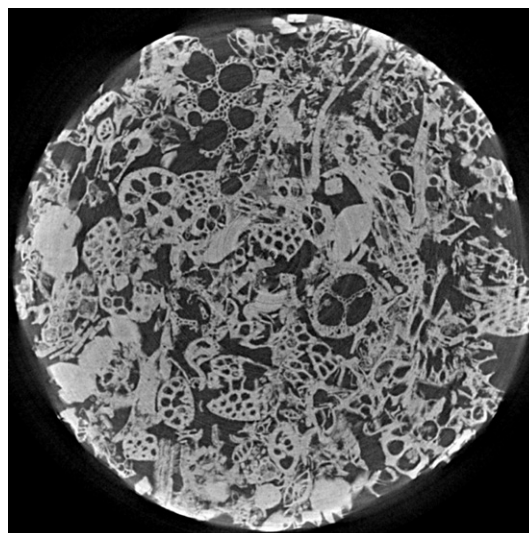

Fig. 1. A lab-based MCT image of Mt Gambier limestone exhibiting beam hardening artifacts, both an increase in apparent attenuation near the sample edge and "streaking" between dense objects. The rock material is pure calcite and the sample is 5 mm in diameter.
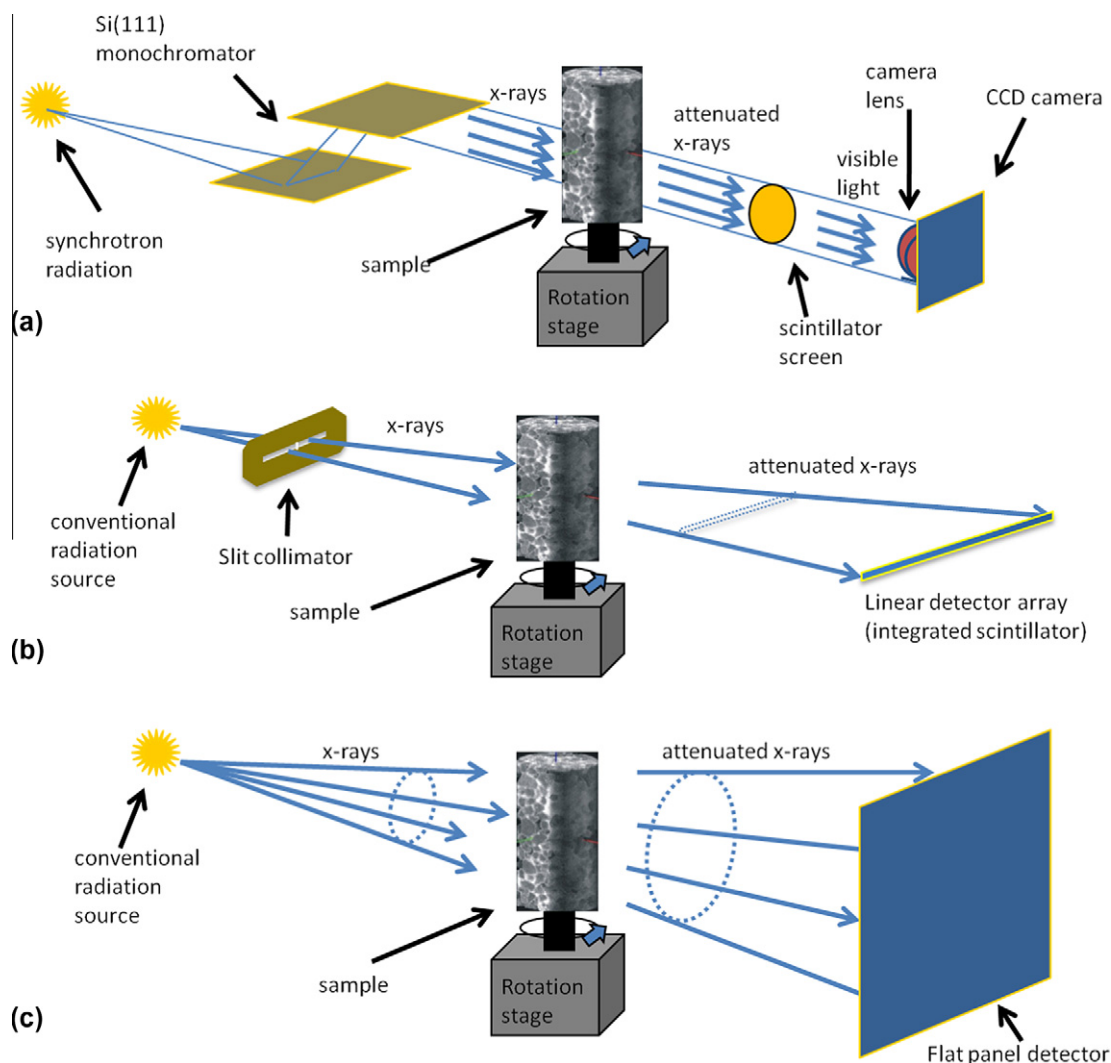
Fig. 2. Typical tomography setup at a synchrotron beam-line (a) and for a microCT system with fan-beam (b) and cone-beam configurations (c).

beam in different ways, so each path through a heterogeneous sample will diverge from the Lambert–Beer law in a different way. A great many methods for partial correction have been proposed. Pre-filtering the beam to remove the lowest energy components is generally considered an essential pre-requisite, while using wedge phantoms is another useful strategy. Ketcham and Carlson [17] contain a good summary of methods used for MCT in 2001. Many methods have since been proposed, mainly in the medical literature, with the preferred methods today being iterative schemes that optimize the consistency between re-projections through the reconstructed object and the experimental projection data. Such an approach was first proposed by Hsieh in 2000 [18]. Post-processing of the tomogram can also be effective when combined with some experimental remedies with Iassonov and Tuller [19] recently proposing a simple but effective method of this type.

2.1.3. Experimental configuration

A typical synchrotron tomography imaging configuration is shown in Fig. 2a. Briefly, the parallel X-rays generated by the bending magnet pass through a monochromator, then through the object of interest, before interacting with a scintillator screen that converts the X-rays to visible light. Imaging optics are often used for magnification before the light is detected by a CCD or CMOS camera. While the specific details of each microtomography

beam-line may differ, all generally work roughly as described in the following which represents the setup at the GSECARS bending magnet beam-line (13 BMD) at the Advanced Photon Source (APS). At GSECARS the bending magnet generates a beam with an intrinsic vertical size of approximately 5 mm in the experimental station, about 55 m from the electron beam source point. When used with a Si [1 1 1] double-crystal monochromator, energies in the range from 7 to 65 keV can be obtained with a beam size up to 50 mm width [20]. However, the beam dimension varies significantly from synchrotron to synchrotron, and the vertical dimension also decreases with increasing energy. The sample is rotated in the beam through a large number of angles (720–1500) where radiographic (2D) projections are captured. The number of angles required for quality images increases with resolution. If insufficient angles are obtained, the system is effectively underdefined, the reconstruction becomes flawed, and the resulting three-dimensional image will be noisy, and the resolution will be negatively affected. Typical acquisition times for a full scan is 5–10 min for synchrotron sources, and from 15 min to 24 h for lab-based systems depending on resolution, energy level, and the chosen exposure time (which affects noise in the images).

The setup for fan-beam and cone-beam lab-based tomography systems is very similar and is illustrated in Fig. 2b and c, respectively. The main difference is the absence of the monochromator and that the geometry of the X-ray beam is either fan-shaped or
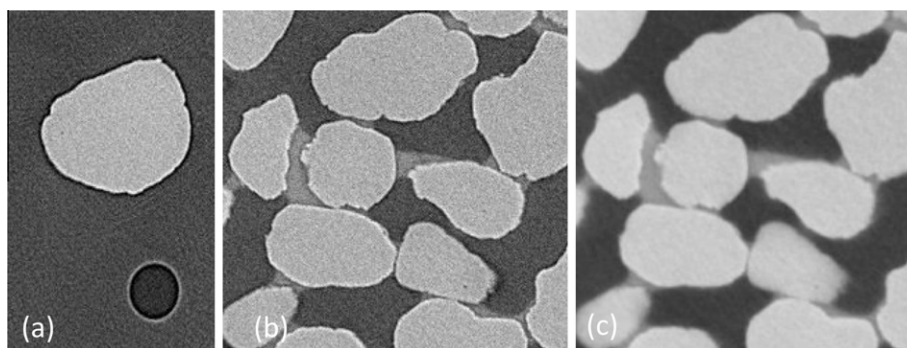
Fig. 3. (a) Polychromatic laboratory MCT Image of single quartz grain (bright) embedded in epoxy with adjacent air bubble (dark) showing significant phase contrast. The two images on the right show a sandstone sample with residual wetting phase between the grains: (b) original with phase contrast, (c) after approximate phase retrieval using the approach of Myers [3] (images courtesy of Glenn Myers, Australian National University).

cone-shaped instead of parallel. However, the scintillation and detection devices used are very similar for the three types of systems, with any differences being due to the need to keep electronic components out of the beam-line at synchrotrons, and the fact that geometric magnification from cone-shaped beam allows efficient large area detectors to be used in lab-scale systems.

Additional details on detectors and scintillation devices are provided under MCT developments in Section 3. General guidelines for experimental design and related constraints related to porous media characterization, flow, and transport are discussed in Section 4.

2.2. Phase contrast microtomography

In many experimental configurations one can safely assume, as above, that the interaction between X-rays and matter is purely one of absorption of the X-ray beam. However, along with X-ray attenuation, X-ray propagation speed is also material-dependent; often a simple function of material density. It is the reverse of visible wavelengths in that X-ray travel faster through more dense materials. For a propagating wave like an X-ray beam, the wavelength varies with changes in speed, causing changes in the relative positions of the wave crests (i.e. changing the *phase* of the wave). According to Snell's law of refraction, this results in a change in the propagation direction, just as light rays are bent by their passage through a lens. One can therefore think of a complex material as a very complex lens that causes small changes in direction. These changes in propagation direction cannot be observed directly since they do not have an immediate effect on the beam intensity. However, as one sees when shining light through a convex lens, after some propagation beyond the object, the change in direction of the light rays cause rays to be slightly converging in some areas and slightly diverging in others. The intensity will be higher where the rays are converging and lower where they are diverging. This intensity variation can be captured by a detector and is called phase contrast. Thus, for non-transparent objects, the intensity distribution beyond the sample is a combination of absorption contrast and phase contrast. Since a longer propagation distance beyond the sample will allow more convergence and divergence to occur, phase contrast becomes more significant as the distance between the sample and detector increases. Phase effects are also more pronounced in higher resolution imaging; see Arhatari [21] for a more complete discussion of phase contrast visibility.

Standard transmission tomography conducted in this regime, where both refraction and absorption contribute to the final image, is called propagation based (or in-line) phase contrast imaging (introduced in [22,23]; well reviewed in [24]). If one can measure both the amplitude and the phase (i.e. direction) of the beam, then tomographic reconstruction can recover variations in both absorption and propagation speed throughout the sample (i.e. the imaginary and real parts of the refractive index). Therefore, the problem of phase-contrast tomography is usually solved by trying to recover phase information in the 2D projections, prior to performing reconstruction. Unfortunately, detectors can only measure intensity, and therefore amplitude, meaning that the beam phase must be inferred, a process known as phase retrieval. Cloetens et al. [25] were able to perform phase retrieval by taking images at four propagation distances, then using an iterative modeling process to estimate the integrated phase change along each ray incident on the detector. They were subsequently able to perform tomographic reconstruction. This type of phase retrieval is relatively straightforward in parallel beams at synchrotron beam-lines but, to our knowledge, this process has not been replicated in cone beam geometry where translating the camera changes ray paths in a non-trivial way.

In-line phase imaging as described above is only the simplest form of phase contrast imaging. The more sophisticated methods can be broken into three categories: interferometry, grating interferometry (differential phase contrast [26]) and diffraction enhanced imaging; for an in-depth review of theory and experiment see [27]. These methods often rely on reasonably coherent and monochromatic illumination and are usually developed with biological applications in mind, since soft organic materials typically offer little absorption contrast. We will therefore not consider these methods further.

In-line phase contrast, on the other hand, which results from simple refraction, occurs even under the polychromatic, incoherent illumination that is produced by simple lab-scale sources. For example, Fig. 3 shows results from a simple radiographs (2D projections) from a simple single propagation distance inline phase contrast experiment conducted at the Australian National University (ANU) lab-scale MCT, with the results of naïve tomographic reconstruction and the partial phase retrieval method from Myers [3]. These exhibit the usual characteristic of phase contrast to "enhance" the edges in both the radiographs and reconstructed tomogram. This results from the fact that rays will diverge slightly behind regions of higher speed such as dense grains, causing the already dark absorption shadow behind such regions to become even darker, particularly at the edges. Since different wavelengths will be differently refracted, calculations are generally very difficult for polychromatic beams, although some headway can be made in the case of monomorphous materials, in which the ratio of the real and imaginary parts of the refractive index is spatially constant [28]. In practice, even at monochromatic synchrotron beam-lines, the existence of phase contrast is usually considered a hindrance, since the mix of refractive and
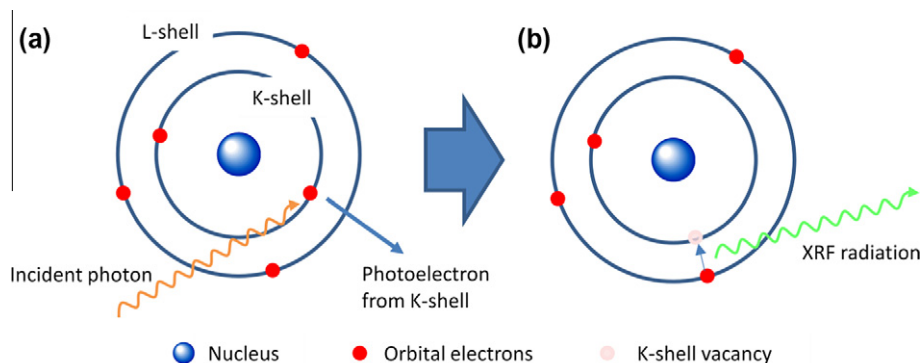
Fig. 4. The principle used in X-ray fluorescence tomography (a) Ejection of an electron from the K-shell of an atom (b) an electron from the L-shell decays back into the K-shell vacancy, simultaneously emitting fluorescence.

absorption effects cannot be untangled for samples of unknown composition, making unique reconstruction impossible. At synchrotrons, phase effects are usually minimized by placing the camera (detector) as close as possible to the source. Burvall et al. [29] have recently summarized non-iterative methods for performing phase retrieval in the context of in-line phase contrast tomographic imaging and found no method to be ideal. Another approach for few-material samples is to regard the under-constrained reconstruction as an exercise in data-constrained modeling, which has been demonstrated for sandstones [30]. This is a rare example of the use of phase contrast for geomaterials.

There are two principal reasons for the slow take-up of phase contrast techniques in the geosciences. Firstly, because geomaterials are typically composed of higher atomic-number elements ($Z \geqslant 13$) they usually exhibit good absorption contrast even for relatively hard X-rays ($E > 50$ keV). Secondly, geomaterials are usually made up of many constituents, so the simpler retrieval techniques are not applicable; one must use one of the more complex techniques that permit quantitative phase retrieval with a minimum of assumptions. However, given the poor absorption contrast between some important constituents of geomaterials, we can see this area growing in the future. For example, quantitative phase imaging has the potential to yield good contrast between water, air and organic matter (including biofilms) within soils, despite their poor absorption contrast to the X-rays typically used in MCT.

2.3. X-ray fluorescence (XRF) microtomography

By far most tomographic measurements are carried out using transmission tomography e.g. [31], yet as early as 1986 it was shown that the elemental sensitivity of fluorescence tomography to high Z trace elements in a low Z matrix was sufficient to use the approach for quantification [32]. In these first XRF measurements the distribution of iron in a honey bee was mapped with a spatial resolution of $\sim$150 μm. With improved optics and employing synchrotron radiation sources, true micrometer resolution is now feasible, and as a result, fluorescence tomography now also has better signal-to-noise ratio for trace element detection. Fluorescence tomography however is very slow compared to transmission tomography because the fluoresced flux is very low, and because of the "scanning" nature of the resulting data collection (using pencil-beam), only a single voxel of data is collected at any one time. For comparison, transmission tomography has a $\sim$10^6 faster collection time because it "scans" all translation positions simultaneously.

The principle behind fluorescence tomography is illustrated in Fig. 4. An electron is brought to an excited energy level (ejected from the atom) by absorbing an X-ray photon (used in transmission tomography) and other electrons subsequently decay back to the lower level shell vacancy, while emitting another photon with an energy that is characteristic of each chemical element. The energy levels in each element therefore lead to a specific X-ray emission spectrum identified as "fluorescence". The fluorescence measurements can therefore reveal the presence of specific elements as well as their elemental state.

X-ray fluorescence (XRF) tomography has become a well-established technique for obtaining accurate information on elemental composition of a variety of materials. Spatially resolved XRF imaging has become a routine technique for performing elemental measurements on heterogeneous samples [33]. The technique is well-suited for studying problems of an environmental nature because it is non-destructive, relatively fast, and allows for analysis of solids with little or no sample preparation.

Fluorescence X-ray tomography is performed with a *pencil-beam* that is scanned across the sample, see Fig. 5. The technique uses a standard undulator-based X-ray microprobe station which provides a very thin X-ray beam. The stage setup is very similar to that used for transmission tomography, yet in addition to transmitted X-rays, fluoresced X-rays are collected with a fluorescence detector, which measures the characteristic X-ray emission lines from de-excitation for each atom. The detectors used in XRF are very different from the imaging detectors discussed in Section 3.5.1
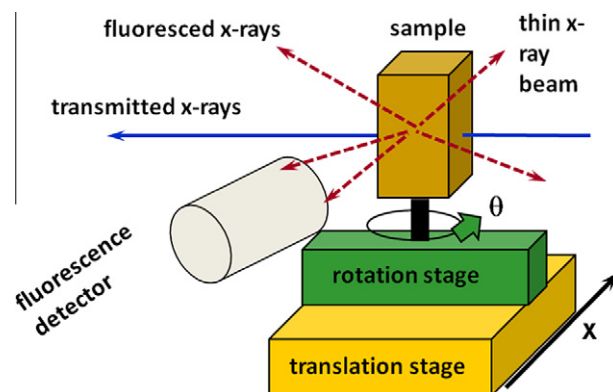

Fig. 5. Typical experimental configuration for XRF tomography: Fluorescence X-ray tomography is performed with a *pencil-beam* scanned across the sample. The sample is rotated around θ and translated in x. (figure courtesy of M. Newville, GSECARS (APS)/Univ. of Chicago).

and are usually based on a single solid-state diode, cooled to reduce noise. When an X-ray photon is incident on the diode, it releases a current pulse of size proportional to the energy of the photon. The sample is rotated, and translated in the *x*-direction. Transmission X-rays can be measured as well to give an overall density tomograph.

The raw fluorescence tomography data consist of elemental fluorescence as a function of position and angle. This data is reconstructed as a virtual slice through the sample. The process can be repeated at different vertical positions to give three-dimensional information. However, because the entire three-dimensional sample has to be scanned with a pencil-beam, the technique is relatively slow. It allows for mapping of elements with atomic number higher than 11 with high precision, and concentrations down to a few parts per million (ppm) can be detected. Measurements can be made on samples down to a few microns in size and samples can be liquids, solids, plant roots and surfaces. It should be mentioned here that XRF has limited penetration depth due to self-absorption of fluorescence X-rays. Thus it is generally difficult to image more than a couple of mm into a sample unless the matrix is very low Z, and as a result it only provides compositional information for regions near the surface of the sample.

3. Evolution of MicroCT and beam-lines

3.1. Evolution of MicroCT

X-ray tubes today use essentially the 1913 design of William Coolidge, a high-vacuum improvement on the cathode ray tube (Crookes tube) used when Wilhelm Röntgen discovered X-rays in 1895. Electrons are generated through the thermionic effect from a heated metallic filament, usually tungsten, under high vacuum, then accelerated and focused onto a target, also usually tungsten. The resolution of the instrument is usually dependent on the size of the point onto which the electrons can be focused.

3D imaging arrived in the late 1960s with the rediscovery by Godfrey Hounsfield and Allan McCormack of the Radon transform, enabling 3D reconstructions of interior structure from multiple radiographs ("projections") taken at different angles [34]. The initial systems used a single photomultiplier tube to detect X-rays (i.e. a 1×1-pixel detector); later systems had linear arrays of photomultiplier tubes, enabling 1D information to be collected in each frame. Laboratory-based *micro*-tomography was pioneered by Sato [35], who produced one 128^2 reconstructed slice of an optical fiber at 6.1 µm voxel size. Very shortly after, Elliott and Dover [36,37] generated 15 µm voxel size images taken of a piece of human femur bone cut into a 0.8 mm cube. In both experiments, the resolution was achieved by collimating the beam through a tiny aperture, then scanning the sample across the beam, acquiring a single pixel of data each time. The time required for the latter experiment was 19 h *per slice*.

In parallel with this work, high intensity microfocus sources were under constant development, with the most important single advance being the development of triode-style guns, in which electrons are initially accelerated through a grid, resulting in a highly collimated beam that can readily be focused. Research into larger systems was driven by industrial nondestructive testing applications, resulting in 150 kV/250 µA systems with a spot size of 50 µm [38]. Smaller systems, built primarily for radiographic microscopy and diffraction crystallography also advanced: in 1981, spot sizes approaching 1 µm were possible with about 15 kV/5 µA (0.1 W) [39].

So, in the early 1980s, microfocus sources with sufficient power and spot size were available, but a reduction was needed in the size of detectors before microtomography would be *practical*. During the 1980s detection technology developed enormously. Seguin et al. [40,41] used a newly developed linear array of 1024 24 µm photodiodes, the data from which was reconstructed to 512^2 slices. Reconstruction was quite sophisticated: deconvolution was used to mitigate against detector cross-talk, and ring-removal software was also incorporated to compensate detector inconsistencies. Aiming at much higher resolutions, Bateman, Rockett and coworkers [42] developed a 128^2 multiwire proportional counter (MWPC) area detector and used it with a microfocus source to generate a 64^3 image of a pistachio nutshell at ∼5 µm resolution; a 2D exposure time of 500 s resulted in a total acquisition time of 12 h.

However, it was charge-coupled-device (CCD) detectors, developed for consumer video cameras, which were, by the end of the 1980s, beginning to transform the field by offering low-cost, high-efficiency area detection of X-rays. Flannery and co-workers at Exxon Research [43] presaged the era of modern MCT by combining a 10 µm micro-focus source with an efficient scintillator-based CCD detector. CCDs were soon making their way into MCT systems in many locations [44,45], and by 1993 all of the required equipment for lab-based MCT was being manufactured commercially [46].

Since this time there has been little advance in the underlying technology, but enormous advances in the imaging quality. The first "modern" laboratory MCT images, of resolution around 10 µm and comprising many hundreds of slices, were published in 1998 [47], with another notable facility constructed by Davis for dental imaging [48]. Ketcham and Carlson [17] provided an excellent summary of the state-of-the-art in imaging down to about 5 µm, as well as explaining experimental techniques for minimizing ring artifacts, that arise from nonuniform sensitivity of detector pixels, and beam hardening artifacts as discussed in Section 2.1.2. This work is still required reading for practitioners. Subsequent advances have come from steady improvement in spatial and temporal stability of the sources, in system alignment and improved detection technologies (see below). The most significant changes, however, are due to the inexorable advances in accessible computer power, so that in 2012 computing capabilities are thousands of times in advance of what was available in 1991. This has provided both the capability to handle high data rates and volumes and the ability to reconstruct and visualize 3D datasets with thousands of voxels on a side. Leveraging local supercomputer facilities, researchers at the Australian National University built a high resolution facility early in the millennium, and were the first to reconstruct and analyse full scale images of 2048^3 voxels [49].

Today, laboratory systems with genuine submicron capabilities have been developed, some with better than 100 nm resolution. Three main configurations are used in systems that seek submicron resolution; a good review can be found in [50]. Firstly, one can use the traditional fine-focus geometry with a "nanofocus" X-ray source, from which the source spot is less than 1 µm. A number of commercial systems like this are available, with better than 1 µm resolution, but reducing the spot size mandates a corresponding quadratic reduction in flux, so image SNR is very low unless very long acquisition times are used. Using the same geometry, but a scanning electron microscope beam as the electron gun, one can generate X-rays of up to 30 kV from a very small spot, with very low fluxes and long acquisition times. A resolution of 50 nm has been demonstrated with this arrangement, with phase contrast effects (see Section 2.3) playing a prominent role [51]. One way to improve the SNR at high resolution is to use helical scanning, in which the object is vertically translated while being rotated, so moving through a spiral path. As discussed in Section 3.4, this allows for theoretically-exact reconstruction so that the cone-angle (the vertical angle that the detector subtends at the source) can be increased beyond the levels allowed by circular scanning [52]. This approach makes system alignment more complex and has so

far been shown to be effective down to about 1 μm voxel size. This approach should be effective for submicron imaging, although to capture sufficient flux, very small working distances are required, with source-sample distance of ∼100 μm for true nanotomography, a distance impossible to achieve with commercially available nanofocus sources today.

A second configuration is that of contact imaging (quasi-parallel configuration), where one places the sample very close to the front face of the detector, so that resolution is limited by the detector rather than the source. While this allows the use of a higher power source, one loses in detection efficiency because of the necessity for a high resolution detector. The fundamental limitation of this setup is the wavelength of the scintillated light (around 500 nm), since the scintillator is optically coupled to a CCD or complementary-metal-oxide-semiconductor (CMOS) detector, as in synchrotrons. At least one commercial system uses this configuration.

A third configuration has been developed with the use of magnifying X-ray optics, particularly an X-ray condenser to direct the beam flux, and a nanofabricated X-ray zone plate to focus the rays onto the detector [53,54]. This system has great potential, since one is able to use a high-power source (although very little of the beam passes through the sample) and there are no working-distance limitations that hamper traditional spatial arrangements. However, the need for a relatively monochromatic beam to enable the zone plate to function properly and the relative inefficiency of the X-ray condenser lens and zone plate mean that the required acquisition times with currently available instruments of this type do not appear to be significantly shorter than with traditional fine-focus systems.

In summary, after four decades of remarkable developments, researchers wishing to make submillimeter images of geomaterials can now choose from an array of instruments on offer from at least 15 vendors worldwide. Instruments range from industrial CT systems, with sources operating at up to 450 keV, that are optimized for scanning large and dense objects, down to true submicron systems for which the samples must be cut down to tiny sub-millimeter pieces.

3.2. Generations of synchrotrons

Natural synchrotron radiation, which is produced when charged particles are accelerated through circular arcs, is as old as the stars. However, man-made, short-wavelength synchrotron radiation generated from purpose-built circular accelerators is little more than half a century old. The first observation, carried out at the General Electric Research Laboratory in Schenectady, New York in 1947, literally was an observation, because it was visible light that was observed. Because synchrotron light can be filtered and used in a wide range of non-destructive, high-resolution, imaging and analysis techniques, purpose-built synchrotron facilities soon appeared and synchrotron radiation has become an essential research tool for a multitude of topics. This has resulted in development of facilities around the world that are continuously evolving to provide synchrotron light in new forms, [55].

First-generation synchrotron light sources were often categorized as parasitic: basically, beam-lines were built onto existing facilities designed for particle physics studies. As a result, synchrotrons were mainly used in the field of particle physics. However, as a side benefit, intense radiation, i.e., synchrotron light is released when high-energy electrons are forced to travel in a circular orbit. With the second generation of synchrotron light sources, facilities were built specifically for the purpose of production of synchrotron radiation (using bending magnets to steer the beam and generate X-rays) and employed electron storage rings. In a storage ring, the electrons circulate continuously at a fixed energy for periods

of up to many hours. The much longer cycles provide a number of advantages such as higher beam currents and hence higher fluxes of radiation, a static radiation spectrum, and greater beam stability. In the storage ring, the electrons are accelerated to near the speed of light using radio-frequency cavities, and magnetic fields to steer and focus the beam. When high-speed electrons are accelerated by a magnetic field they emit electromagnetic radiation. The radiation is projected at a tangent to the electron storage ring and the emitted radiation is directed as a beam to each experimental station. A beam-line may originate at bending magnets which are used to "bend" the trajectory of the particles in the storage ring; or at insertion devices (undulators and wigglers), which are located in the straight sections of the storage ring. Both devices accelerate electrons and thus produce radiation. The main difference between insertion devices and bending magnets pertains to the spatial distribution and spectrum of light that is emitted. Undulators emit light that is highly collimated in both the vertical and horizontal directions (typically less than 0.05 mrad) and occupies a narrow wavelength bandwidth. Bending magnets (and wigglers) emit a wide horizontal fan (several mrad), with a narrower vertical opening angle (0.1–0.3 mrad) and a continuous broad band of wavelengths. In terms of applications, wigglers produce X-ray spectra similar to those of bending magnets, but with flux that is increased by the number of magnetic poles in the wiggler, and as a result will have a different characteristic energy. Undulators have distinct advantages in terms of tomographic imaging because the intensity (photon per unit area per unit energy bandwidth) of the beam can be up to 1000 times greater than a bending magnet. This allows for very high resolution imaging and provides for very short acquisition times, however the total field of view is only 1–2 mm, and the energy range is lower (leading to constraints in terms of sample penetration, and use of contrast agents).

The radiation emitted spans an enormous range in wavelength, and includes radio waves, visible light, and X-rays. Two qualities of an X-ray beam, flux and brilliance, are needed for innovative experimentation. Flux describes the number of photons per second passing through a defined area, and brilliance is a measure of the intensity and directionality of the X-ray beam. It determines the smallest spot onto which an X-ray beam can be focused, and thus contributes to the resolution with which measurements can be made. The radiation produced by synchrotrons is millions of times brighter (e.g. more brilliant) than conventional laboratory X-ray tubes, see Fig. 6.

As the second-generation sources were coming on line in the 1980s it was discovered that insertion devices could be implemented and operated such that X-rays several orders of magnitude more powerful than bending magnet beam-lines on the same storage ring could be generated, see Fig. 6. Thus, third-generation storage rings were designed to accommodate large numbers of insertion devices to maximize flux and brilliance. Laboratories around the world are now working on developing fourth-generation light sources, which are likely to utilize hard X-ray free-electron lasers (FEL). These have the potential to increase the brilliance by 4–5 orders of magnitude compared to an undulator, [56]. Fig. 6 shows a comparison of the brilliance of various generations of synchrotrons, to that of a lab-scale X-ray tube, and the potential promised by the new FELs that are under development.

3.3. Synchrotron beam-lines

What all these sources have in common is very high emitted flux, and this is what renders synchrotron tomography such a powerful tool for imaging. Yet, the insertion devices produce much brighter radiation, and have therefore been the focus of development since the 1980s. As seen from Fig. 7, the development of
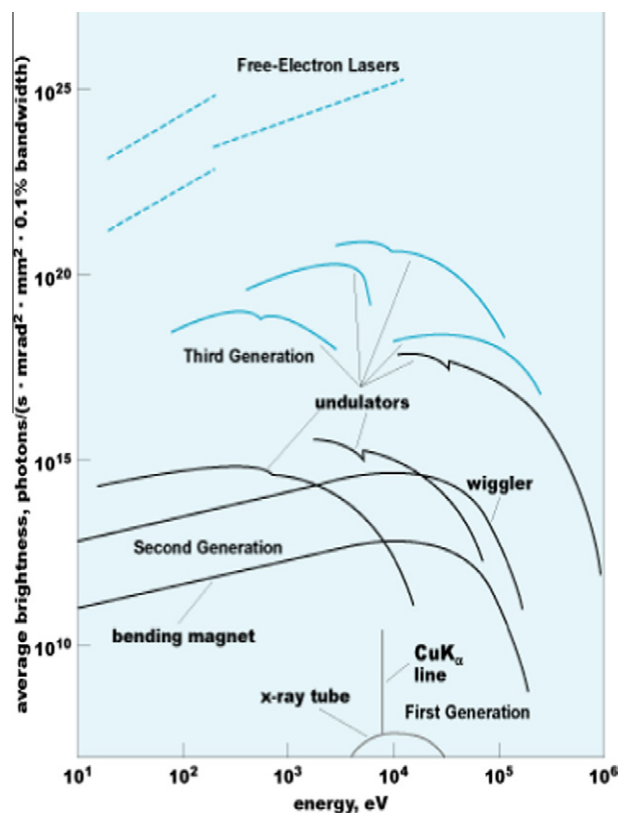
Fig. 6. Representative average brightness of synchrotron radiation sources and free-electron lasers as a function of photon energy. Present and extrapolated performances are shown. From Schlachter et al. [2] with permission.
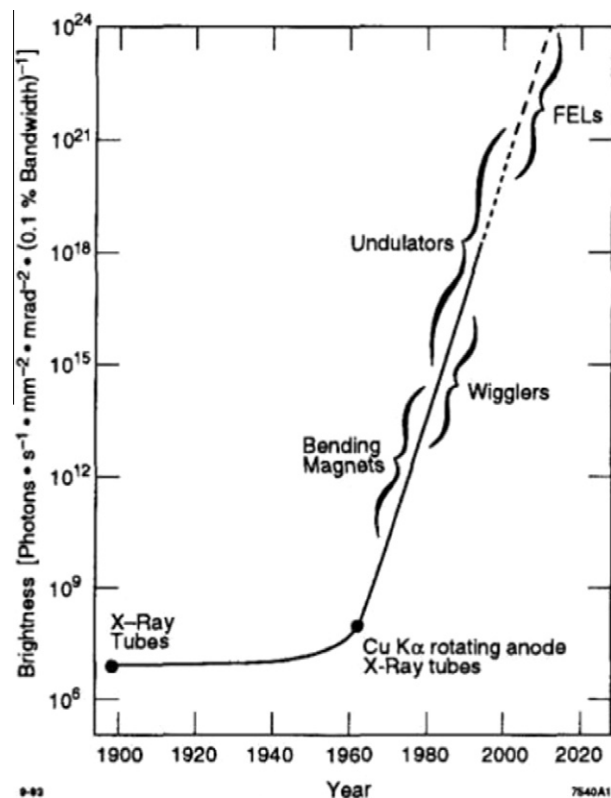

Fig. 7. Spectral brightness of X-ray sources as a function of time. From [1].

undulator and wiggler beams-lines drastically improved the brightness of generated X-rays, however, bending magnets continue to perform well as the "working horse" beam-line for many imaging applications, and have themselves seen development, such as the newer superbend magnets.

One of the first published synchrotron-based _micro_tomography experiments was carried out at the Russian particle collider facility VEPP-4 [57] in 1986, followed shortly by development of a micro-tomography beam-line (jointly with researchers at Lawrence Livermore National Lab) at DORIS/HASYLAB in Germany in 1986 [58], and the National Synchrotron Light Source (NSLS) in the USA in 1987 [43,59,60]. Since then microtomography capabilities have been developed at a number of the synchrotrons in the USA: Advanced light Source (ALS), Advanced Photon Source (APS), Center for Advanced Microstructure and Devices (CAMD) and at the European Synchrotron Radiation Facility (ESRF) in France, Swiss Light Source (SLS) in Switzerland, at Spring-8 in Japan, at Deutsches Elektronen-Synchrotron (DESY) in Germany, and at the Diamond Light Source in the UK.

3.3.1. Beam-line design

In brief terms, a beam-line consists of three main components, the front-end where X-rays exit the storage ring, the beam-line optics, and the experimental station. Before the X-rays get to the experimental station, they pass through an array of sophisticated components that are designed to protect the users from radiation, and the storage ring from vacuum failure (which would shut down the entire storage ring). Monochromators consisting of pairs of Si or Ge crystals are often an integral part of synchrotron beam-lines and are used routinely for absorption (transmission) tomography. By changing the angle of the two crystals relative to the incoming white synchrotron light, monochromatized light is selected: Following Bragg's law, each component wavelength of the white synchrotron radiation directed at a single crystal of known orientation and d-spacing (the interatomic spacing), will be diffracted at a specific angle. Monochromators make use of this fact to selectively remove radiation outside a narrow tunable energy range, and pass only the radiation of interest. Because of the high photon flux of synchrotrons, the flux after this monochromatization is still sufficient for fast and high-resolution imaging, whereas a similar procedure would deplete a laboratory X-ray source so much that long scan times and noisy images would result. Monochromatic radiation facilitates energy-specific imaging, and the photoelectric effect can be used to great advantage to enhance the contrast of a phase (e.g. a fluid phase) that would otherwise have a very low X-ray cross section (low absorption) and therefore would not be easily distinguished in a tomographic image.

In addition to monochromators, many beam-lines are equipped with a focusing mirror to increase the photon flux, and to produce micrometer-sized focused beams needed for instance for X-ray fluorescence tomography; magnifying X-ray optics such as Kirk-Baez mirrors, compound refractive lenses, or Fresnel zone plates [56] are used. Zone plates have recently also been implemented for absorption tomography and facilitates resolution near the diffraction-limit for X-rays (several tens of nm) [61] (because of the diffraction limit one cannot image things that are much smaller than the wavelength of the light used, in this case X-rays). Without the use of zone plates, the spatial resolution is limited to 1 μm or slightly less due to the spatial resolution of the detector or to the deflection of X-rays [61].

3.4. Reconstruction methods

Hounsfield's first tomograph used algebraic reconstruction, which involves solving the entire linear system of equations resulting from the discrete Radon transform [34]. This is extremely

computationally intensive and only practical for small data sets and parallel or fan beam arrangements where one can reconstruct each slice independently. For single-pixel detectors like in Hounsfield's system, one gets effectively a parallel beam by translating the sample from one pixel to the next, but data acquisition is extremely inefficient. Fan beam geometry, which arises from use of a linear detector array with sample translation, is also equivalent to parallel beam, with simple data reordering required to map one onto the other. For these fan- and parallel-beam geometries, where 3D reconstruction can be treated as a series of independent 2D slice reconstructions, and the X-ray transform and the Radon transform coincide, high-quality and relatively efficient reconstruction methods of the filtered backprojection (FBP) type were developed during the 1970s [62].

Although fan beam acquisition with collimated linear detectors is still preferred for high-energy (e.g. 450 keV) industrial imaging where X-ray-matter interaction is dominated by Compton scattering, cone beam geometry is generally preferred, since acquiring a full 2D projection at a time allows great improvements in acquisition time and image quality. Cone beam reconstruction is far more difficult since the X-ray transform does not coincide with the Radon transform and in fact cone-beam CT with circular scanning collects insufficient data to fully characterize the sample. Feldkamp et al. [63] provided the first workable FBP-type reconstruction method for cone beam geometries. This method, although an approximation that breaks down at high cone angles, remains dominant today, with alternative methods failing to match the reconstructed image quality.

It was long recognized that helical scanning offered the best prospect of improving this state of affairs. However, researchers were unable to devise methods that could scan long objects or develop an FBP-type method for helical cone-beam geometry. After decades of intense research, Katsevich in [297] published the first workable reconstruction method for helical cone-beam tomography, indeed the first exact FBP-type reconstruction method for any form of cone beam tomography. Practical implementation of exact reconstruction for micro-tomography turned out to be challenging, with the first implementation for MCT not achieved until 2010 [52].

Backprojection is a perfect algorithm to be implemented on highly parallel computers and graphics processing units (GPUs), since the backprojection of each ray can be performed in arbitrary order, with each ray being independent of all others. This was quickly realized by researchers and industry, with graphics cards being rapidly co-opted from 2004 to perform reconstruction [64]. Reconstruction can be performed about 50 times faster on a GPU, so that desktop computers shipped with laboratory systems can, in 2012, perform full 2000^3 reconstructions inside 1 h.

With computing power no longer being a major restriction, there is a renewed interest in the more computationally demanding iterative reconstruction techniques like the simultaneous iterative reconstruction technique (SIRT) [65]. For example, Myers et al. [66] uses a constrained SIRT-based method for studying two-phase flow in a bead pack that combines reconstruction and segmentation.

3.5. Future trends

3.5.1. Detectors

X-ray detector technology is today quite mature, with detection efficiencies largely reaching fundamental limits, although potential readout speed increases may further reduce acquisition times at synchrotron beam-lines. Current detectors in use are CCD, CMOS and amorphous-Silicon (a-Si). At synchrotrons, CCDs are being replaced by CMOS which provides faster readout, while for lab-based systems a-Si is most common due to its high detective quantum efficiency (DQE). Looking to the future, hybrid CMOS photon counting detectors appear to offer the best prospect for future breakthroughs. These devices are able to achieve energy selectivity by thresholding the electrical pulse that is produced by the arrival of a single X-ray photon. This works since higher energy photons generate larger electrical pulses. There are two basic technologies, both using hybrid CMOS detectors where an array of silicon/GaAs/CdTe photodiodes that detects the X-rays is coupled using solder bumps on the chip's reverse side to CMOS readout electronics. The Medipix detectors, developed for particle physics applications, are part of a large consortium centered at CERN, and in Medipix3 form are 256×256 pixel detectors of 55 µm, with some energy selectivity [67,68]. The other, more mature technology is the PILATUS detector, developed for crystallography at the Paul Scherrer Institute [69]. These detectors consist of 487×195 172 µm pixels that can be tiled into arrays up to 6 megapixels, and have been demonstrated to deliver high performance in medical imaging for accelerating voltages up to 40 kV. Both detector types have demonstrated excellent radiation hardness for use directly in beam-lines, but cannot be used for direct synchrotron imaging since single photon counting electronics only functions up to count rates of about 10^7 photons/s. Such rates are adequate for lab-based systems, but far too slow for synchrotron use. In both devices there is zero readout noise, which is significant for crystallography and high energy physics, but irrelevant for imaging applications where, using today's detectors, the only source of noise is shot noise arising from finite photon numbers.

As electronics technology improves, one can expect the count rate and energy selectivity of these detectors to advance. This may get to the point where a polychromatic beam becomes an asset rather than a liability, allowing phase retrieval (see Section 2.3) and genuine elemental discrimination. At the moment, price is another significant limit on this technology, but its potential value in medical imaging may one day see detectors like these in mass production, which could prove revolutionary for MCT imaging.

3.5.2. Sources

X-ray lab sources have reached a power density limit of about $2 \text{ W}/\mu\text{m}^2$, and while rotating anode sources offer some scope to increase this somewhat, this is close to the fundamental limit for such systems, as target heating leads to material vaporization at higher power levels.

One intriguing idea to avoid this problem is to use a continuous jet of liquid metal as the target for the electron beam [70]. This has been developed into a commercial product that uses a Gallium jet, with strong emission at 9 keV, providing a partially monochromatic source with a spot size of 6.5 µm and a power density of $8 \text{ W}/\mu\text{m}^2$ [71,72], roughly a factor of 4 higher than conventional lab-scale sources. Theoretical limits for these systems are much higher, but the complexities of managing a jet currently prevent the systems from reaching their potential. At this time it is difficult to tell whether the technical obstacles of this technology can be overcome. More prosaically, some groups are building high-precision rotating anode instruments, pushing the spot size from such instruments down towards the single micron scale.

There are a number of other promising technologies for developing high quality lab-scale X-ray sources. Interacting a high-power pulsed laser with a beam of high-energy particles can be used to produce monochromatic X-rays of moderate flux via the inverse Compton effect [73–75]. Also known as laser Compton sources, these are expensive and complex devices which to date produce inadequate flux to be genuinely useful, but certainly have good potential to bridge the gap between bench-top and synchrotron systems. Another instrument constructed with the same goal is the family of MIRRORCLE tabletop synchrotrons from Japan [76], which have a 1.2 m diameter storage ring at energies up to 20 MeV.

A beamed micro-focus X-ray source can be constructed by placing a micron-sized target in the beam-line, and after monochromation the beam retains a relatively high flux with excellent coherence. Another alternative is to make use of the X-rays that are generated from the plasma cloud that is created when a high-power pulsed laser is directed at a solid target [77]. Beams from these systems are quasi-monochromatic but are limited by the laser power, and so far deliver very little flux.

As mentioned previously, the major new X-ray source technology for frontier science is the X-ray free electron laser, which promises orders of magnitude improvements in flux, monochromaticity, and coherence. Certainly, such a source offers massive potential for tomographic imaging, but the major driver for their construction is the possibility of single-molecule crystallography. It is unclear whether beam-lines on these extremely expensive facilities will ever be made available for micron-scale tomography.

4. Combining experiment and imaging

Many beam-lines and commercial lab-based MCT systems now have a sufficiently large working space for investigators to fit their various pieces of equipment and measurement devices right on the tomography stage. However, there are still both commercial and synchrotron systems for which this is not the case, and the process-oriented experiments that can be carried out using these systems may therefore be constrained by the size of the working space, and or by the ability to run electrical connections and fluid flow lines etc. to and from the core holder, fluid flow cell, or other experimental system. An additional complexity is the need for attached electronics or fluid lines to be able to rotate 180° or even 360° with the sample as it rotates in the beam. In the following we provide an overview of some of the types of experiments that have been, or could be, carried out while also acquiring tomographic image data.

Ideally, the process-oriented experiments can be carried out in the beam-line so that all imaging can be performed without displacing the sample, resulting in a sequence of 3D images that are all perfectly aligned with one another. Such perfect alignment is essential if the images are to be subtracted or otherwise referenced to another, which is the frequent foundation for further analysis. However, there are many occasions when it is inconvenient or impossible to carry out the experiments inside the instrument, e.g. reactive flow experiments that take days or weeks to run. The experimental procedure then involves alternating steps of imaging and ex situ sample modification. In this case, it is effectively impossible to return the sample, with micron precision, to the same position and orientation, and the images taken need to be aligned (registered) with one another. If the sample has not been deformed, then rigid body registration can be used to achieve voxel-perfect alignment of all images. The general problem of rigid body registration in 3D is computationally complex, particularly if the images have been scaled differently. Ketcham and Iturrino developed a simple and efficient method that allowed them to study fluid penetration into volcanic rocks [78], while Latham et al. developed a scalable parallel registration toolkit that was applicable to a wider range of situations [79]. If the sample has been deformed by the experiments, rigid-body registration is no longer applicable since voxel-level alignment is not possible. In this case, the technique of digital volume correlation [80] can be used to generate a map showing the displacement vector of each voxel (i.e. a full strain map), this is discussed further in Section 4.4.

4.1. Temperature and pressure

For many applications constant temperature is a requirement, and this can only be accommodated if the tomography system is either temperature-controlled or if the hutch is sufficiently large that temperature does not increase during scanning. If this is not the case, one might for instance see movement of interfaces in a multi-phase system in response to variations in interfacial tension with temperature. High pressure and elevated temperature experimentation is becoming increasingly desirable as researchers probe flow and transport systems related to the deeper subsurface environment: oil recovery processes, geothermal energy recovery, and geologic sequestration of CO_2.

Likely because it is a rather complicated process, to our knowledge, only very limited experimentation at pressure and temperature has been achieved for tomography with micron-scale resolution, and attempting pore-scale resolving capabilities. Silin et al. [81] reported probably the first micron-scale resolution, high-pressure imaging experiments. A 5.5-mm diameter wide and 20-mm long Frio sandstone core was saturated with water and supercritical CO_2, and imaged at the Advanced Light Source with a resulting voxel size of 4.5 μm. Silin et al. [81] reported a number of technical difficulties with the setup, including the small size and thus weakness of such a thin sample. They also found it difficult to acquire an image with sufficient contrast between the pore fluids. As a consequence, the images were noisy and somewhat unsuitable for a routine thresholding algorithm. The relatively modest concentration of KI (0.5 M) used by Silin et al. [81] may be the reason why insufficient contrast was achieved between water and supercritical CO_2. They concluded that the quality of the output was far from perfect, yet their attempt of obtaining such data was the first reported in the literature. The latest study on imaging pore-scale fluid distributions at temperature and pressure corresponding to CO_2 being in its supercritical state was recently published by Martin Blunt's group at Imperial College [82]. Their attempt was more successful in that they were able to measure trapped supercritical CO_2 clusters in a sandstone core and quantify their size distribution.

In the last year or two, various research groups have built tomography-compatible Hassler type core holders (made from Al, PEEK, and Be) for performing pore-scale imaging at elevated temperature and pressure, and we should see a number of studies being published in the coming few years. A significant body of work exists for experiments at elevated temperature and pressure on rock cores with diameters on the order of inches and using medical and lab-based CT scanners, but the 5–10 μm resolution needed for pore-scale research was not obtained in these studies and they are therefore not discussed further.

A group of researchers at Météo-France, CNRM/CEN developed a cryo-stat around the turn of the millennium to investigate snow phenomena with microtomography at the ESRF. Snow undergoes a structure metamorphism that is governed by surface parameters, such as the surface area or the local curvature. X-ray tomography was applied to natural snow at beam-line ID19 at the ESRF in order to measure local 3D curvature as a governing parameter of metamorphism, and thereby evaluate the pore-scale effect of snow metamorphism on avalanche risk prediction. The tomography compatible cryo-stat was designed to ensure sample temperatures below −40 °C. This involved cycling liquid and gaseous nitrogen through the cryo-stat while it was mounted on the tomography stage. We refer to [83–86] for additional details of the cryo-stat approach to snow imaging. Meanwhile another group at Institute for Snow and Avalanche Research in Davos, Switzerland also developed techniques for imaging snow, in this case using a snow breeder to induce temperature gradients in the sample while scanning it successively [87–89]. Heggli et al. from that same group reported on tomographic imaging where all the instruments were operated in a cold room at −15 °C to −20 °C. Therefore, further cooling of the sample was not necessary [90].

4.2. Flow and transport

For many years, most flow and transport experiments were carried out in a separate laboratory and the specimen, core holder, flow cell, etc. was then transported to the scanning facility for evaluation. In recent years, it has become much more feasible to perform the experiments on the scanning stage (in the hutch) such that disturbances from transportation can be avoided and registration issues are simplified (e.g. [91,92]. If sufficient access to the facility can be secured, this is much preferred. This allows for imaging of multiple fluids, concurrent measurement of pressure, temperature and other relevant variables during flow, which can be controlled by a high-precision syringe or piston pump. Stray radiation, even at a synchrotron, does no harm to most electronic equipment, so data can be collected in the hutch while imaging is carried out. The only constraint for multi-phase flow experiments is that in order to get high quality images, the systems needs to be at or near equilibrium so that no interfaces move during the time it takes to scan. Otherwise, the images will be blurry and contain artifacts because the projection data become inconsistent with no single solution of the reconstruction problem. Very recently, new efforts have been made to scan systems outside of equilibrium, this is further discussed below.

4.3. Electrical and acoustic measurements

Similarly to flow and transport experiments, it is possible to make a multitude of other relevant measurements while the sample is being scanned. Among them are electrical conductivity and resistivity, and acoustic measurements. Many studies have been reported where electrical and acoustic emissions are measured in separate experiments (e.g. [93–96], several of these probing Archie's Law relationships and coupling the tomographic measurements with other investigative tools (NMR, SEM, ERT tomography, etc.), but only few have reported carrying out the entire sequence of measurements simultaneously on the scanning stage. Redwan and Rammlmeir [97] however, reported making simultaneous measurement of electrical conductivity and water saturation via X-ray tomography using an experimental setup involving use of a geophysical foil that allowed them to monitor level dependent changes of electrical conductivity during scanning.

4.4. Mechanical loading

Using specially designed loading stages (manufactured by many of the commercial CT vendors) it is possible to simultaneously image multiple fluid distributions and make electrical resistivity and acoustic measurements during a core flooding event at elevated pressures and temperatures (as mentioned above). If combined with a triaxial loading cell, it is also possible to track the evolution of fractures and fluid flow during loading as well as monitoring the acoustic signal resulting from the load.

As mentioned in the introduction to this section, strain fields resulting from mechanical load can be calculated using digital image correlation techniques based on displacement field measurement and subvolume tracking. The strain fields are then calculated from the displacement fields by gradient estimation techniques, e.g. [98]. Using digital image correlation applied to lab-scale MCT images, Peth et al. [99] calculated the displacement fields of soils under compressive loading after being exposed to successive swelling/shrinkage cycles. Along similar lines, [100] imaged limestone samples before and after hydraulic fracturing and were able to describe the fracture propagation as a function of the heterogeneity and roughness of the sample. Gates et al.

[101] developed speed and efficiency improvements to a three-dimensional digital volume correlation (DVC) algorithm, which measures displacement and strain fields in three dimensions in a given material. As a result DVC can be performed with resolution comparable to 2D digital image correlation, and in a time frame similar to the image acquisition time.

Monsen and Johnstad [102] investigated relationships between velocity and fluid saturation at reservoir stress levels during flooding experiments. They used a high pressure capacity core holder and were thereby able to simultaneously image fluid distribution and measure acoustic velocities. Other subsurface and flow related mechanical load studies have been reported by Louis et al. [103], Charalampidou et al. [104], Raynaud et al. [105], David et al. [106,107], but the majority of these studies have not taken advantage of the capability to do all the measurements simultaneously, likely because the trade-off in experimental complexity was not warranted for what was sought in terms of discovery. In very recent work, Wang et al. [108] did make high-pressure and high temperature tomographic measurements during large-scale deformation.

4.5. Imaging of dynamic processes

As mentioned above, tomography, by its very nature, is limited to situations where the scanned object does not change during the time it takes to scan it. However, if scan times can be decreased sufficiently, and flow is adequately slow, then fast or dynamic tomography may be an option. This has been under development at synchrotron facilities for a number of years; the high flux meaning that the main requirement is a detector with high read-out speeds. At synchrotrons, monochromators are normally used to maximize signal-to-noise ratio (SNR) and to facilitate straightforward quantitative analysis. For performing fast tomography, the energy spectrum is either filtered slightly (called pink beam), or the entire white beam spectrum used to enable 3D data acquisition times below 10 s, as reported by Di Michiel et al. at the ESRF [109]. The sample specimen is also rotated continuously in the beam to allow 2D exposure times in the millisecond range. Since that first reported experiment, a number of other synchrotron beam-lines have developed similar capabilities, e.g. [110–113]. The latest white beam imaging development at the Swiss Light Source is aiming at sub-second temporal resolution in 3D while maintaining image sizes of 2048^3 [113].

In a recent study, Myers et al. [66] presented a new method for dynamic MCT imaging – i.e. the imaging of a continuously changing sample – using a lab-based MCT imaging system. They employed what is called discrete tomography (DT), in which it is assumed *a priori* that a static sample may be represented using only a few (usually two) gray levels, a valid assumption when considering only the *changes* between one moment and the next. DT algorithms allow one to reconstruct samples from far fewer radiographs than is normally needed, leading to corresponding reductions in scan time and X-ray dose. The approach uses a sophisticated reconstruction algorithm that makes appropriate use of *a priori* information, for instance about the static pore geometry, and the incompressible nature of the fluids involved. In this manner, it is possible to reconstruct a 4D dataset from projections of a continually evolving sample at a high spatial and temporal resolution. Myers et al. presented proof-of-concept experimental data and reconstructions for a multi-phase flow system, and demonstrated order-of-magnitude improvements in time resolution and X-ray dose when compared to conventional reconstruction methods [66]. This technique is equally applicable to lab-based and synchrotron imaging.

4.6. Multi-scale imaging

Multi-scale imaging capabilities, i.e., the development and integration of a range of experimental and computational tools which can assist one in probing the structure of materials across many decades of scale in an integrated fashion has been an area of focus for several groups in recent years. The ANU group, for example, has developed a multi-scale imaging system that incorporates back-scattered scanning electron microscopy (BSEM), and focused ion beam SEM (FIBSEM) in the analysis of rocks, [8], see Fig. 8(i). This technique is particularly suitable for examining carbonates because of their multi-modal pore structure which can span seven decades in terms of length scale (from 10 nm to 10 cm). In their 2009 publication, Sok et al. [8] report on both plug to pore scale registration in 3D, as well as pore-scale to submicron scale registration of features. The plug to pore scale approach requires that one or more subsets of the sample originally imaged (at the scale of 4 cm and at 20 μm/pixel) have to be reimaged with MCT at a smaller sample volume (5 mm and at 2.5 μm/pixel), and that the data be perfectly registered and integrated. The pore-scale to submicron scale registration was done by cutting the subsamples and preparing thin sections from the original field of view of the MCT images. The thin sections were then imaged with BSEM and registered to the MCT image using the approach of [79] for direct comparison between the two image modalities. Finally, in order to estimate reservoir properties for complex materials such as carbonate and mudstones, FIBSEM images were also obtained at voxel resolutions of 50 nm. The ANU group reported initial attempts to co-register the 3D MCT data to the 3D FIBSEM data, however, given the limited sample size of the FIBSEM data, Sok et al. [8] report that this has been quite difficult. A longer term goal of this group is to undertake complete multi-scale registration from the whole core and/or plug scale through the MCT length scale and down to the submicron (SEM or FIBSEM) scale. Along somewhat similar lines, Grader et al. [114] also reported on multi-scale imaging, where a carbonate sample was imaged at increasingly finer resolution (smaller volume) via physical sub-sampling.

5. Analysis and quantification

5.1. Segmentation

While it is possible to base quantitative analyses directly on the grayscale images that are produced from tomography, the goal of MCT is usually to image at sufficient resolution to capture the geometry of the features (see Fig. 9), and most analysis therefore commences by performing segmentation. The word *segmentation* is somewhat overloaded, since in the field of image processing it
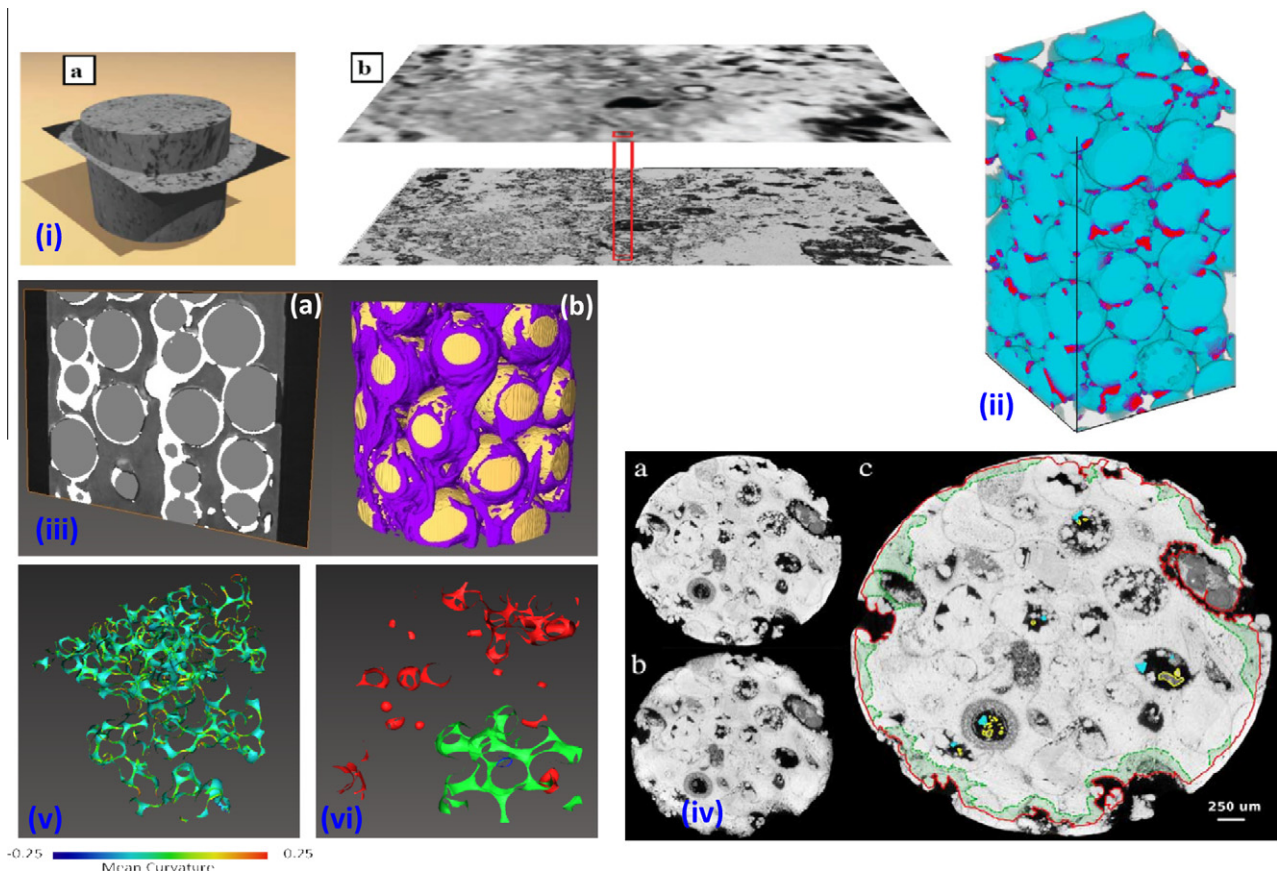

Fig. 8. Examples of frontier research performed with X-ray microtomography (i) multi-scale imaging; (a) schematic of 2D SEM to 3D micro-CT registration: (b) example of the mapping of the microporosity from a registered slice of a 3D CT image (2.85 μm voxels; upper region) to the higher resolution information (0.25 μm pixels) in the SEM image (lower region), from [8]; (ii) colloids: Three-dimensional representation of a column internal volume of dimension 0.6 × 0.6 × 1.2 mm showing glass spheres (blue) and colloidal zirconia deposits (red), from [9] with permission; (iii) biofilms; biofilms imaged with MCT using a BaSO$_4$ suspension for distinguishing the biofilm from solids and water (a) a 2D slice showing the biofilm (white), solids (light grey) and water (darker grey); (b) 3D rendering of the biofilm (purple) against the solids (glass bead pack in yellow), imaged at 4.5 microns, based on work from [10,11]; (iv) reactive transport; (a) initial state, (b) final state after 48 hours in 10 atm CO$_2$, (c) red line (superimposed on initial state) shows new boundary after dissolution; green area shows microporous regions where porosity is increased. Imaged at 2.8 μm, from [12]; (v) curvature estimation: curvature of wetting-nonwetting fluid interface in glass-bead pack, imaged at 13 μm, from [13]; (vi) phase connectivity: rendering of connected vs. disconnected phase in multi-phase images: (green) interface between connected wetting and nonwetting phases, (red) interface between connected wetting and disconnected nonwetting phases, and (blue) interface between disconnected wetting and connected nonwetting (blue), also from [13]. (For interpretation of the references to colour in this figure legend, the reader is referred to the web version of this article.)
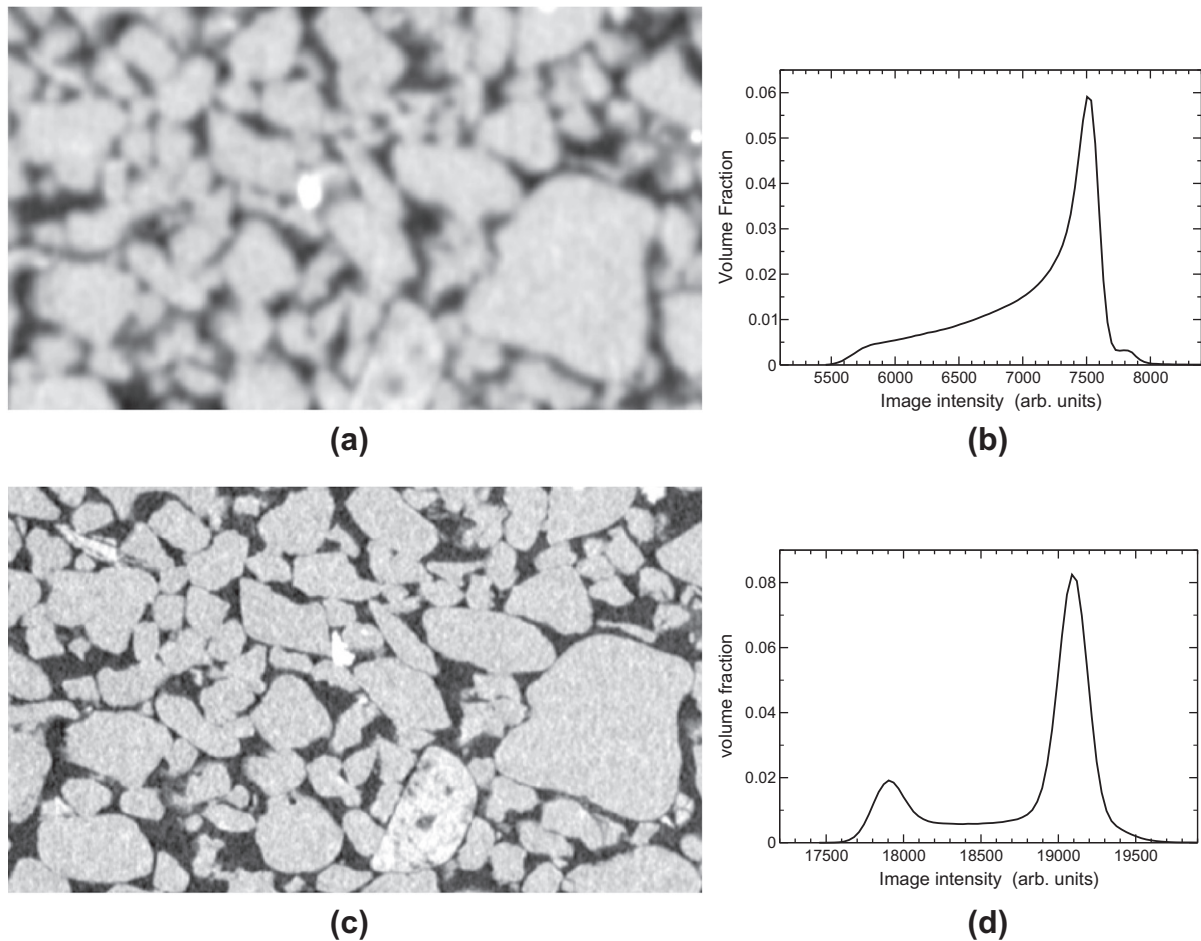
Fig. 9. (a) Image of unconsolidated sand at 28 μm, with insufficient resolution to capture the geometry of features and (b) corresponding single-peaked (monomodal) histogram. (c) Image of the same region at 10 microns with sufficient resolution showing (d) clear double-peaked (bimodal) histogram. From Varslot [7].

often means decomposing an object into *segments.* In the field of tomography, however, it has come to mean the identification of discrete materials in an image, frequently the binarization of an image into just two materials, represented by black and white.

In an absorption contrast tomogram, the value associated with each voxel is proportional to its X-ray attenuation, which is a function of density, atomic number and the energy of the incident X-rays. Therefore, the primary information to be used when trying to distinguish between the different materials in a sample is simply the voxel intensity value. For this reason, most studies to this day will segment their dataset by simply choosing an intensity threshold, with values below the threshold assigned to one phase/material, and those above the threshold assigned to the other phase. While automated methods exist for selecting this threshold, the two most popular being by Otsu [115] (2-phase systems only) and Ridler and Calvard [116] (also called *k*-means clustering, for any number of phases), the threshold is usually chosen by hand. Recent advances in imaging hardware mean that for simple materials (e.g. bead packs), the grayscale image can be sufficiently clean that thresholding can be used. There is universal agreement among researchers that automated methods are preferable in theory, since they both save operator time, while eliminating operator bias or subjectivity. In the research group where one of us (APS) works, operator subjectivity in the selection of manual thresholds has repeatedly been shown to be significant. The problem, however, is that automated histogram *thresholding-based* methods do not give consistent results when applied to slightly

different images of the same material. Iassonov et al. [117] gave a very good review of segmentation methods which also compares between automatic thresholding methods and some noise-tolerant segmentation schemes. This study found that automated schemes gave inconsistent results and concluded that automated ("unsupervised") schemes cannot yet be used with any confidence. However, Porter and Wildenschild [118] have shown, using synchrotron data, that for sufficiently high quality images collected in sequence, automated segmentation can work very well.

While thresholding is appealing for its simplicity, it is intolerant of many imaging artifacts, particularly image noise. Therefore, images acquired of complex materials, on older systems, or with acquisition time constraints usually contain significant amounts of image noise, so direct application of a threshold often results in a poor quality segmentation (see Fig. 10b). As illustrated in Fig. 10c–f, there are three ways to resolve this: (a) perform noise-reduction on the grayscale data before segmentation (b) perform morphological noise-reduction on the binarized data after segmentation, or (c) use a noise-tolerant segmentation method. Option (a) is almost universally preferred over (b) since filtering of the grayscale image is more flexible than filtering segmented data, and has been used widely, although option (c) is also popular, as discussed below. Thousands of methods for performing edge-preserving noise reduction, also called image restoration, have been published, the majority directed towards 2D imaging. These methods are usually too computationally intensive to apply to very large images; methods with complexity of $O(N)$ or $O(N \log N)$,
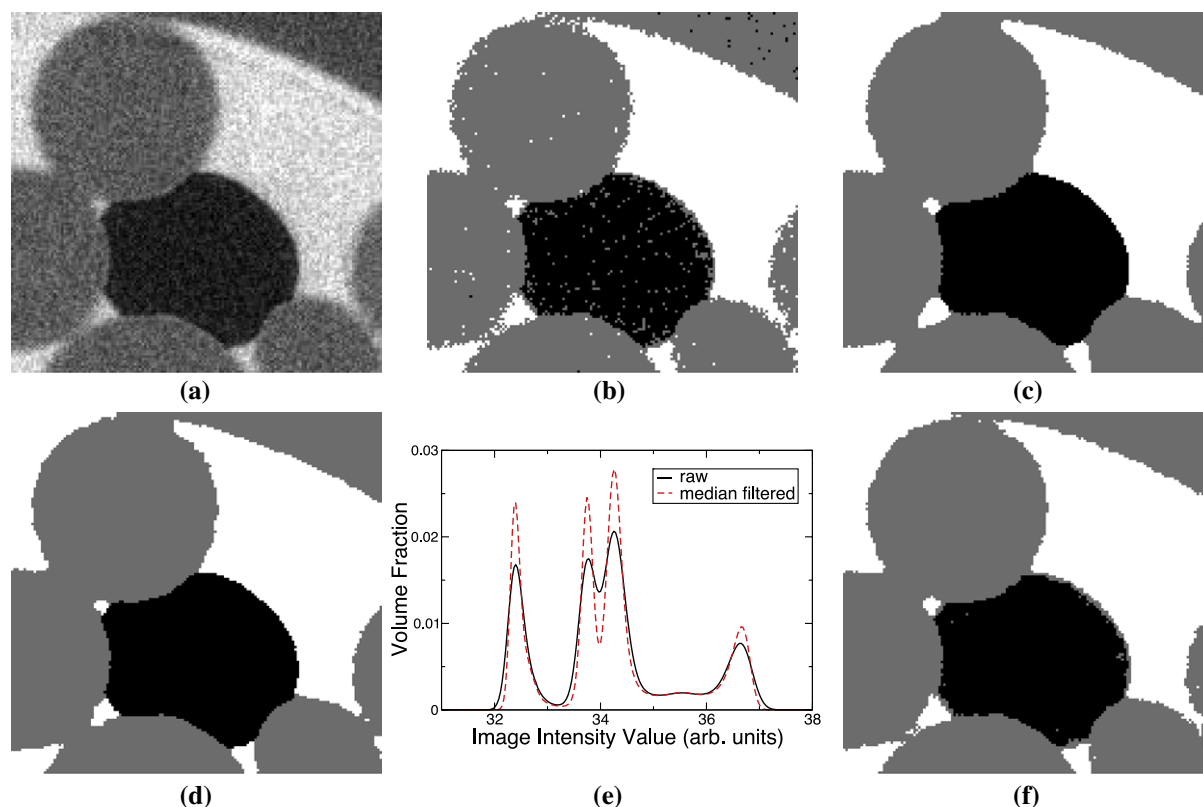
Fig. 10. Filtering and segmentation scenarios on image of a glass bead pack partially saturated with CsCl-doped water. (a) Unfiltered grayscale tomogram (b) thresholding segmentation of (a), showing significant noise. (c) Majority filtering of (b), showing noise suppression but unavoidable smooth surfaces. (d) Noise-tolerant segmentation of (a) using method from Sheppard [5]; phase boundaries remain noisy. (e) Effect of median filtering on histogram of intensity values showing sharpening of peaks associated with each phase. The two overlapping peaks of similar attenuation are from two different types of glass. (f) Thresholding segmentation of median-filtered data, showing some noise suppression.

where N is the number of voxels, are normally acceptable whereas $O(N^2)$ methods are infeasible. Wavelet methods have been widely used as variations of image compression techniques (see, e.g. [119]), but are usually complex to implement, rather computationally intensive and require tuning for specific problems. The dominant methods today are based on either anisotropic diffusion [120] or Bayesian information theoretic techniques [121,122]. While these methods can assist as pre-segmentation steps, they will always reduce the information content of an image, usually resulting in loss or distortion of small features. Simple median filtering is also commonly used on poor quality images.

Unfortunately, (or, perhaps fortunately) dozens of methods now exist specifically for the segmentation of microtomographic images, each developed to address a particular shortcoming of other available methods, often with noise tolerance in mind. Watershed-transform based methods are pre-eminent in medical imaging, usually with some user-supervision. However they are rarely used for MCT, where sample complexity usually renders user-supervised methods less suitable. In the geosciences, the method of indicator kriging [123] stands out as being widely used, and in recent comparative studies on real [117] and synthetic [124] images, it was judged to perform well for a small set of images that included data from granular and soil samples. Indicator kriging was devised for noisy images and applied in this context by Prodanovic et al. [125] and also found to perform well on relatively clean synchrotron images of multi-fluid phase images by Porter and Wildenschild [118].

There are, however, severe difficulties with evaluating the quality of segmentation methods. Firstly, there is no "right answer" for a real tomographic image of a representative sample. Secondly, a method that is optimal for a particular sample type on a particular instrument will not be optimal on other systems. For example, images of granular packings are often of very high quality, with almost all voxels unambiguously in one phase or another. Images of soil samples, on the other hand, contain dozens of different materials (with different mineralogy) whose attenuation differences may be smaller than the image noise, often arranged in features smaller than the image voxel size. The segmentation task for these two cases is very different.

The dramatic advances in image quality over the past decade have also greatly changed the problems that segmentation needs to solve. In the 1990s, faced with images that were extremely noisy, the primary goal of segmentation methods was to produce a 2-phase (binary) image that was not overcome by the image noise. Today, with sharp, low-noise images, one often wishes to distinguish between numerous different minerals, and to capture features only a few voxels in size. Indeed, a voxel pattern that would have been correctly discarded as noise in an image from 1999 can be a real but small feature in a high-fidelity image in 2012. The main result of the improved images is that simple voxel intensities can be relied on more than ever, and that filtering and segmentation methods which use inter-voxel correlations are less likely to be appropriate.

Amongst traditional segmentation methods, Bayesian methods using Markov random fields [126] appear to be the most promising, and certainly have the best theoretical foundation. These methods minimize a global cost function, and thus end up being very computationally intensive. Highly efficient "max-flow mincut" algorithms from graph theory are an elegant way to solve this problem [127,128], but are limited to binary segmentation. Level

sets ("active contours" and "snakes") are another closely related global optimization method that can also work well for moderate sized images [129,130]. There is continual progress in this field, particularly in the area of automatic parameter selection and better use of neighborhood information [131,132]. In most modern approaches, the task is one of first estimating the mean and variance of each phase, then classifying the voxels between these phases. Increasing computing power is making these methods more feasible, although to our knowledge they have not yet been applied to tomographic images of geomaterials.

The image sharpness and SNR of modern images is such that the information content of each grayscale voxel is equivalent to more than one "bit", so that any binary segmentation throws away hard-won information. In this context, the challenge is to develop segmentation methods that retain more than a single data bit per voxel, which has long been a goal in the analysis of brain MRI images, where partial volume effects are severe. One can allow phase mixtures in each voxel [133], or explicitly consider subvoxels [134]. Most work is in MRI brain imaging, but a similar approach has been applied to MCT images of trabecular bone [135] or for non-destructive testing [136]. Mohebi and Ioannidis have proposed a more sophisticated approach for geomaterials, combining segmentation and microstructure reconstruction in a Bayesian framework [137]. This method is currently limited for computational reasons to 2D images only. Ketcham and coworkers [138], tackling the simpler problem of estimating the sub-voxel width of a single rock fracture imaged with MCT, achieved consistent results between instruments and across resolutions, which certainly represents another major goal for future research. Directly generating 2D surface meshes from grayscale images during segmentation is another approach to avoid voxel-scale resolution limitations. It has been efficiently developed for brain imaging [139], where the topology of the desired object is known in advance; dealing with unknown topology remains largely unsolved.

Another approach, in very limited use for the time being, is to combine segmentation with reconstruction, extending the principles of binary tomography, pioneered by Herman and Kuba [140] and developed by Batenburg [141]. This is only useful when one has *a priori* information that the sample is indeed composed only of several discrete phases, but has seen several applications to the geosciences in the context of dynamic tomography [66] and phase contrast imaging [30].

5.2. Morphology and topology

The great advantage of microtomography over conventional microscopy is the level of quantitative information that can be derived from a full 3D property map. From the outset, those generating 3D microscale images applied fairly advanced techniques for quantifying characteristics of interest, with several groups ending up developing truly sophisticated software. In this section we outline some of the most important methods that have been found to be generally useful. Many more measures have been derived for specific applications, some of which will be described in Section 6 of this paper.

5.2.1. Measures on grayscale data

It would be ideal to be able to perform analysis directly on the grayscale image as produced by the reconstruction. There are, however, a number of severe limitations on the value of measures calculated directly on grayscales. Firstly, the grayscale units produced by MCT instruments are different from one sample to another and between facilities. Indeed, unless the identical X-ray frequency was used, it is impossible to exactly correlate the CT grayscale units. Secondly, even if the grayscale units could be placed on approximately the same scale, the measures of interest

will almost always be affected by image noise, and by edge sharpness (i.e. the effective system modulation transfer function (MTF)). Thirdly, the high dynamic range of MCT images means that one can image materials with tiny but very highly attenuating inclusions that dominate typical grayscale measures. For example, zircon can be $40\times$ more attenuating than silica, meaning small pieces of zircon will have a disproportionate effect on image statistics.

For these reasons, few measures are performed directly on raw tomographic data. Those that are, usually relate to measuring heterogeneity (spatial nonuniformity) or anisotropy (directional nonuniformity). Pre-eminent among these are methods related to the Fourier transform, such as the 2-point correlation function or its close relation, the variogram. These functions show the level of statistical correlation between image values at spatially separated points. One can estimate the correlation length in the sample by fitting a decaying exponential to the correlation functions, although in a complex multi-scale material the fit will be poor. More often these functions are used to estimate the distance at which the correlations drop to zero, this being a measure for the largest length scales present in the material and an indication of the size of the representative elementary volume (REV). Anisotropy can be quantified through the Fourier transform itself or the 3D autocorrelation function, by measuring radial asymmetry in the transform images.

Other measures are also used for quantifying heterogeneity and anisotropy on grayscale data. For example, simple spatial averaging over boxes of increasing size: the average grayscale value in each box trends to a single constant as the box side length is increased past the length scale of heterogeneity in the material. An elegant method for capturing heterogeneity, particularly effective in granular systems, is to the use the Radon [142] or the Hough transform [143] to measure how the integrated grayscale values along lines or planes depends on their orientation.

Sometimes, one is obliged to make use of the grayscale values. This is, for example, often the case in the presence of extensive sub-resolution microporosity, for which partial volume effects render segmentation meaningless. This is a situation very familiar to those working in conventional mm-resolution CT. One approach begins with a two-level thresholding, or, equivalently, three-phase segmentation where the imaged is partitioned into phase 1, phase 2 and an "in between" phase. One then performs a linear grayscale transformation on the in-between values to generate a grayscale image which numerically represents the volume fraction of each material within in each voxel [8].

5.2.2. Measures on segmented data

Multipoint statistics, epitomized by the 2-point correlation function, are even more useful when applied to binarized data than to grayscale data since their behavior can be rigorously linked to geometry, with only finite voxel size playing a role. Torquato [144] provides a good summary of various correlation measures and how they can be related to the physics of various processes. The use of X-ray transform measures in the characterization of anisotropy is also equally valid, and has been used to measure fiber orientation in images of composite materials [145].

Integral geometry is a fascinating branch of mathematics [146] that was brought to the attention of the physics community by Mecke and Wagner, initially for the analysis of cosmic structure using astronomical sky survey data [147,148]. The main measures of interest from integral geometry are the four Quermass integrals (or Minkowski functionals), that capture (1) volume, (2) surface area, (3) integrated mean curvature and (4) integrated Gauss curvature or Euler characteristic. This set of four additive measures can easily be computed from local properties. Remarkably, it can be shown that *any* additive property of an object can be expressed as a linear combination of its Quermass integrals. Therefore, they

are expected to be of value in studying properties that show additive characteristics, such as heat capacity (exactly additive) and resistance. Schladitz has recently provided a review of the Quermass integrals and related geometric techniques for analysis of structure in microtomography [149], while Lehmann [150] and Vogel [151] have made use of these integrals as part of a general geometric analysis of soil. In another recent work, Schröder-Turk et al. have extended Quermass integrals to tensorial quantities [152], which have potential value for studying anisotropy and higher order surface structure.

The Euler characteristic itself deserves special mention, as it spans geometry and topology. While it arises as the fourth Quermass integral, it is also a topological invariant, meaning that the Euler characteristic of an object remains unchanged under any continuous deformation of the object. Indeed, topological structure – the set of topologically invariant measures of an object – is often closely related to physical properties, and one often wishes to be able to measure more topological invariants. To move beyond the Euler characteristic it is natural to consider the family of Betti numbers β_i from homology theory. For a three-dimensional object, β_0 is the number of distinct objects (i.e. connected components), β_1 is the number of "handles" (for a single object, equal to the genus of the object's surface), while β_2 is the number of isolated voids (or cavities). Fig. 11 shows the Betti numbers for a number of simple objects. For such objects the Euler characteristic χ is given by $\chi = \beta_0 - \beta_1 + \beta_2$ from which one can see that the Betti numbers can be thought of as a decomposition of the Euler characteristic into its elemental constituents. β_1 is difficult to calculate in isolation but can be determined by rearranging this relation into $\beta_1 = \beta_0 + \beta_2 - \chi$; the RHS terms here are all straightforward to calculate [153]. Unfortunately, topological measures are extremely noise sensitive, suffering from the shortcoming that small features are weighted equally with large features. This can be partially circumvented through the use of majority filters, but a better solution would be to use topological persistence methods which provide a measure for the significance of topological features and a means to remove less significant features [154]. It turns out that there are a number of complications associated with the application of these techniques to structures extracted from 3D digital images, which have only recently been satisfactorily resolved [155,156]. The new topological techniques arising from these works are also likely to lead to better and more robust skeletonization, along the lines of similar work by Glantz and Hilpert [157,158].

The family of *distance transforms* provides another important way to characterize structure. The most common of these is the Euclidean distance transform, which assigns to every voxel in the pore space (or, more generally, the object) the distance to the nearest non-pore-space voxel. This can equivalently be viewed as being, for each voxel, the radius of largest sphere that fits into the pore space and which is centered at that voxel. Yet another perspective comes from mathematical morphology [159]: the isosurface of the Euclidean distance transform at value r is the boundary of the object that results from eroding the pore space using as a structuring element a sphere of radius r. Another important distance transform results, not from erosion, but from morphological opening by Euclidean spheres. This transform is often called the covering radius transform as it assigns to each voxel the largest pore-space-fitting sphere that covers that voxel, which means that voxels with a value less than r are locations ("crevices") in the pore space that cannot be accessed by a sphere of radius r. Its isosurfaces are surfaces whose larger principal curvature is constant. This transform is therefore of particular interest for the study of 2-phase flow as its isosurfaces are closely related to the fluid–fluid interfaces. Its principle shortcoming is that by using Euclidean spheres it generates surfaces that are insensitive to the smaller of the two principle curvatures (see Section 5.4.2) and will often make poor predictions, particularly where the fluid–fluid interface would be saddle-shaped. After being introduced for studying 2-phase flow by Hazlett [160], this approach was refined by Hilpert and Miller [161] and soon used in the analysis of MCT images [150,162]. Having performed transforms such as these, one can use them as the basis for further analysis (see below) or collect statistics on the images themselves, such as the distribution of distance values.

The important problem of relating the microstructure of bone to its properties has received a great deal of attention in the literature and for this reason many of the measures used in the geosciences are taken from bone research. Here, 3D image data was generated through serial sectioning before MCT became available. One of the key anisotropy measures from the bone literature is the mean intercept length (MIL) tensor [163]. Tensors like this for characterizing anisotropy are called fabric tensors; their eigenvalues and eigenvectors can be used to identify the principal directions and degree of anisotropy. Related fabric tensors are the star volume distribution, star line distribution and volume orientation [164,165]. Another powerful measure from the bone literature is the topological surface-to-curve ratio, which is derived by thinning the object to a skeleton that consists of both lines and sheet-like structures then determine their relative abundance of these two feature types [166].

It is standard, when analyzing geomaterials, to think in terms of the representative elementary volume (REV). This assumes that the material is homogeneous when viewed at a sufficiently large scale, or at least that if one measures a physical property of interest on samples larger than the REV, then the scatter in results is tolerably low. If, instead, one considers the samples to be fractal in nature,
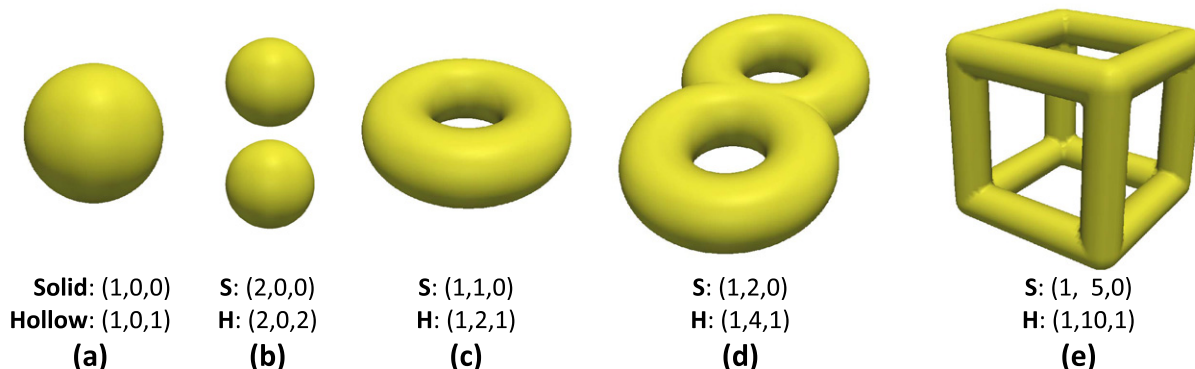

Solid: (1,0,0)	S: (2,0,0)	S: (1,1,0)	S: (1,2,0)	S: (1, 5,0)
Hollow: (1,0,1)	H: (2,0,2)	H: (1,2,1)	H: (1,4,1)	H: (1,10,1)
(a)	**(b)**	**(c)**	**(d)**	**(e)**

Fig. 11. Betti numbers listed as a triplet (β_1, β_2, β_3) for a number of simple three-dimensional objects considered as solid (S) or hollow (H). (a) Single sphere, (b) two disjoint spheres, (c) torus, (d) double torus, (e) cubic frame.
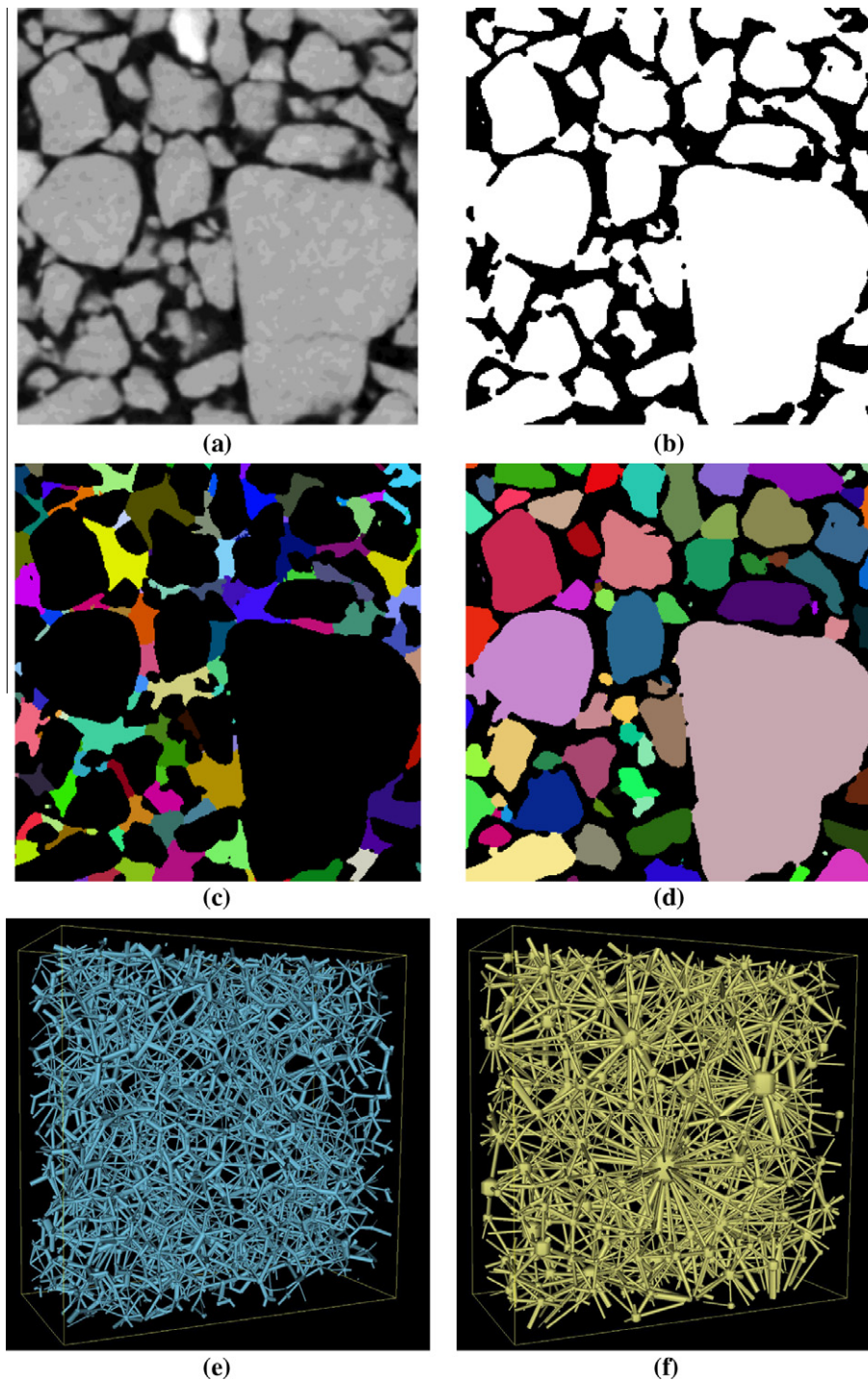
Fig. 12. Examples of partitioning and subsequent ball-and-stick network construction, applied to an unconsolidated sand imaged at 2.8 μm. (a) Zoom into slice from original gray-scale tomogram (b) segmented image. (c) Partition of the pore space using watershed transform and subsequent region merging, where each region is given its own randomly chosen color. (d) Partition of the grain space. (e) Equivalent pore-network of 3D region surrounding the 2D slice shown in (a)–(d). Each node in the network corresponds to a single coloured region in the pore partition. (f) Equivalent grain network. (For interpretation of the references to colour in this figure legend, the reader is referred to the web version of this article.)

then there will be no reduction in the scatter as the sample size is increased. This behavior is characterized by performing scaling analyses, as applied, for example, by Iglauer et al. [167] and Liu and Regenauer-Lieb [168]. This latter work also considers the percolation properties of subvolumes, i.e. whether pore space contains a connected spanning component. How the likelihood of percolation scales with subvolume size is a simple measure with implications for the scaling of transport properties.

5.2.3. Partitioning schemes and measures on partitioned data

The measures described above represent integrated properties of a segmented image as a whole, and while they are extremely useful, it is difficult to relate these directly to micro-scale shape on the complex labyrinthine structure revealed by MCT images. Therefore, one often wishes to break down the complex structure of interest into simpler building blocks. Doing this enables one to study the properties of these blocks, and then also study the

manner in which they are connected. This approach is clearly of particular value for granular materials, which naturally decompose into simple building blocks, as seen in Fig. 12a–d, and is also the principle behind pore-network extraction, which is discussed in Section 6.

Early studies that wished to identify discrete components in 3D images were often obliged to perform laborious manual analyses due to the lack of available computer software and hardware. For example, Denison et al. [169] went through the 3D MCT volume slice-by-slice, manually drawing around the periphery of each crystal of interest. Stacking the 2D slices back together was then used to determine many geometric properties of each crystallite. Today there are a number of different schemes used for partitioning, all operating on the principle that the boundaries between regions (i.e. the grain boundaries) should be located at constrictions. While, as described in Section 6, several different approaches still flourish for partitioning the pore space for the purpose of pore-network generation, for grain space decomposition the watershed method is pre-eminent. This technique, from the field of morphological image processing, works by first taking a distance transform of the segmented image, then applying the watershed transform to that image, Beucher and Lantuejoul [170]. The watershed transformation is applied as if the distance function was inverted, so that a watershed "basin" (corresponding to a grain) surrounds each local maximum of the distance transform. Direct implementation of the watershed transform will result in one grain associated with every local maximum, which results in far too many grains since surface roughness can cause additional local maxima. Therefore, all the proposed algorithms that use this method apply some additional processing, either before or after the watershed, to reduce the number of grains [171–173]. Fig. 12 shows the results of applying watershed partitioning and region merging on the pore and grain space of an unconsolidated sand. One major weakness of all these partitioning schemes proposed to date is the use of spherical structuring elements, which breaks down when the grain shapes are very oblate or prolate [173].

Once the partitioning has been performed, one can build a network (or graph) in which the nodes are the regions (grains or pore bodies) and with links connecting adjacent nodes with a common boundary, as shown in Fig. 12e and f. Having done this, the first property to investigate is the coordination number distribution, where the coordination number is the number of neighbors of each node in the network. For studying both the mechanical properties of granulates, and the transport properties of porous materials, this number is considered to be of critical importance. Other, more sophisticated techniques for characterizing networks exist, with off-diagonal network complexity [174] being one promising measure of network topology.

As mentioned earlier, a principal benefit of decomposing an object into simple pieces is that it enables the detailed study of the shape of the individual pieces. In the context of a granular material, this means finding descriptors of the grain shapes. After calculating volume and centre of mass (zeroth and first moments of the particle shape), the next step is to calculate the tensor of inertia – the second moment – which is equivalent to fitting an ellipse to the particle surface [175]. This can immediately be used to give measures of grain fabric and to characterize orientation anisotropy, but clearly captures only a tiny fraction of information about the grain's shape. In the field of sedimentology [176] the shape of grains is determined from manual analysis of 2D thin section images, or visual inspection of particles in sieves. The two standard measures are sphericity, which can be well defined in 3D, and roundness, which attempts to measure the angularity of the grain and which is rather poorly defined.

An elegant approach for providing a more complete description of grain shape is to expand the grain surface in spherical harmonic functions about its center of mass [177]. This has now been applied to a range of materials [178–180], usually related to the structure of cement, and primarily to provide more accurate measures of length, width and thickness than can be obtained from ellipse fitting. So, while this technique is very effective for capturing features with low angular frequency (i.e. the lower-order angular moments), the issue of capturing particle angularity remains largely an open question. We note that this is not the full story of describing local geometry; good examples showing the sort of geometric and topological characterization that can be performed on partitioned data are also to be found in the pore-network construction literature [125,172,173,181–188].

5.3. Porosity, fluid saturation and distribution

Some of the simpler measurements that can be made from tomographic *pore-scale* images are sample porosity, fluid saturations, and their spatial distributions, classification of pores into matrix and macropores, etc. Porosity and saturation can be estimated by simply counting the number of voxels assigned to each phase during segmentation. This works regardless of the number of phases present in the images, as long as they are reliably segmented. For lower resolution images, i.e., beyond the pore-scale, these types of measures can only be obtained as averages on a per-slice basis or for an entire imaged specimen. In many cases, medial-axis based network generating algorithms such as 3DMA Rock [181,189,190] are used to produce statistical representations of the imaged pore space for use in numerical network models, see additional content in Section 6.1.

5.4. Surface triangulation area and curvature estimation

5.4.1. Constructing surface triangulations from image data

For many of the more complex measures such as solid surface area, fluid–fluid interfacial area and surface curvatures, simply counting voxel faces results in a systematic, orientation dependent overestimation of surface area that cannot be corrected or improved by finer sampling. One should therefore construct a triangulation of the surface, using surface mesh generating techniques such as the widely used marching cubes (MC) algorithm [191], which produces a triangle mesh by computing isosurfaces from grayscale image data. MC works in a purely local manner, stepping through the image in cubes bounded by 8 voxels, linearly interpolating within these cubes to identify surface patches, then connecting these patches to produce a surface representation. More modern triangulation methods such as Delaunay refinement meshing (DRM) [192,193] produce much higher quality surface triangulations than methods based on MC, although they are much more difficult to implement. Flin et al. [84], as part of introducing a new method to compute surface normals, made a comparison of MC with DRM applied to segmented MCT images of snow, and found DRM to be decisively superior in terms of surface normals and total area.

Once a triangulated (or polygonized) surface has been created, it is possible to directly measure the surface area by adding up the area of all the triangles, and also calculate curvatures from the surface normals, or using discrete curvature operators (see below). The MC method has been shown to yield inaccurate measures of surface area when applied to segmented image data [194], arising from the fact that the surface triangles can only be oriented parallel, or at 45° to the grid axes. While smoothing the binarized image data back to grayscale values can partially resolve this issue, it results in undesirable volume and topology changes.

One major obstacle with the use of standard surface generation methods for the analysis of fluid interfaces inside porous media is that the resultant images have three phases (e.g. levels 0, 1 and 2

for air, water and solid respectively) for which simple isosurfaces (level cuts) do not correspond to boundaries between any two phases. For example, one cannot find the air–water interface – the boundary between phases 0 and 1 – by forming the 0.5 level cut. Doing this will yield instead the surface separating phase 0 from phases 1 and 2 combined. Porter and Wildenschild [118] have shown that one can calculate fluid–fluid interfacial areas from three-phase images with good accuracy by forming linear combinations of the areas of the isosurfaces. However, for more complete surface characterization, or even adequate visualization, one must properly delineate each boundary. It is also important to pay special attention to regions where all three phases meet, known as three-phase contact lines or common curves. To this end, McClure et al. developed an extension of the MC method designed to deal specifically with three-phase systems, called porous media marching cubes (PMMC) [195]. These extensions enable PMMC to deal correctly with three phase contact lines, and were shown to deliver accurate surface areas and three-phase contact line lengths, although good results were only obtained after smoothing the binarized image values. Higher order interpolation schemes were also proposed for PMMC, which have the potential to reduce artifacts associated with binarized image data. Porter and Wildenschild [118] compared both a modified MC and the PMMC approach to measured values from MCT data and obtained similar surface area estimates from both methods. It should also be stressed that not all studies rely on surface extraction, for example Rodriguez et al. [196] recently extracted three-phase contact line information from segmented multiphase images and multiphase simulation data using a medial-axis-type thinning technique.

5.4.2. Curvatures

Unlike a line, whose curvature is simply the inverse of the radius, a smooth surface has two independent curvature values at each point, usually represented by either the two principal curvatures or the Gauss and mean curvature. Being differential properties, curvatures are difficult to measure and are extremely noise sensitive. This can be particularly problematic at the edge of the image, or at three-phase contact lines, where large local bending can influence the global average. Many methods have been developed to calculate the curvature of a triangular mesh. Flynn and Jain provided an early review of several techniques that involves fitting a paraboloid to a patch of the surface around each point [197]. The primary conclusion of this work is that the results are poor unless the surface has been smoothed. Many techniques have been developed since then, notable being the efficient method of Taubin [198] that calculates the curvatures without explicit fitting. A much more recent review of techniques was performed by Magid et al. [199], which concluded that techniques that performed best for the Gauss curvature performed worst for mean curvature and vice versa.

As an alternative to fitting a continuous function to the surface locally, one can use discrete formulations of the curvature operators, an approach understood by Santalo in the 1960s and is mentioned in his book on integral geometry [146]. A complete description of the approach can be found in Meyer [200]. Many other methods have been proposed for curvature estimation, often aiming to be robust to surface roughness. Rusinkiewicz [201] provides a clear review of existing techniques and proposes a promising method which has not, to our knowledge, been tested on tomographic data.

Finally, one can also measure curvatures from segmented images by first constructing a grayscale signed distance function, then using the level set formulation to estimate the curvatures of the zero-isosurface of this grayscale function [202]. McClure [195] calculates curvatures using a variant of this method in which one constructs a grayscale function by smoothing the segmented

image. Note that in these cases the triangulated surface is not used at all.

There have been very few studies in which curvatures have been calculated from tomographic image data. Flin [203] constructed a curvature-flow algorithm for describing the compaction of snow, then compared model results to synchrotron image data, in which the mean curvature of the ice surfaces was calculated using a simple orthogonal parabola fitting method [203]. In very recent work, Armstrong et al. [13] measured fluid–fluid interfacial curvature for a two-phase fluid system of oil and water using the paraboloid fitting method mentioned above. An example showing these estimated curvatures superimposed onto the oil-water interfaces is included in Fig. 8(v). They used the calculated curvatures to estimate capillary pressure via the Young–LaPlace equation and compared these estimates to capillary pressures measured with a pressure transducer. The results were highly encouraging for modest curvatures, i.e., at relatively high saturations, but they concluded that because curvature estimation is so sensitive to noise and overall image quality, even better results could be obtained at low saturation if the analysis was performed on data with higher resolution and with better SNR. The data analyzed was collected at 11 μm and using only 720 angles at a synchrotron beam-line, so generating better data to accomplish this is quite feasible.

6. Applications

6.1. Pore network generation

It is often desirable to construct from a sample's pore space a representative network of pore bodies linked by pore throats, both in order to characterize its structure and to enable pore-network modeling of two-phase flow [204]. This is, of course, not the only way to simulate 2-phase fluid displacements from MCT images – since the pioneering work by Auzerais and co-workers [205], direct solution of immiscible 2-phase Stokes flow has been widely explored, with the lattice Boltzmann (LB) method generally pre-eminent [206–208], although the volume of fluids method is seeing some use. While direct simulation requires minimal assumptions and admits scalable implementations, it is extremely computationally demanding, limited in scale and becomes less efficient for very low capillary numbers. For low capillary numbers where interfacial curvature and contact angle are the primary drivers, the level set method is another powerful numerical tool [209]. Finally, it should be mentioned that for capillary-dominated 2-phase primary drainage under strongly wet conditions it is also possible to perform drainage simulations directly, through an elegant morphological analysis of the pore space revealed by the image [160,161]. Some interesting comparisons between these methods in sand packs have been made by Vogel and co-workers [210,211], who found that the network models show significant errors under imbibition, while the full 2-phase flow solvers gave poorer results at low water saturations.

The first published works on extraction of structure from 3D images was from Lindquist and co-workers who developed sophisticated image analysis software including pore-network extraction based on skeletonization using the medial axis transform, and applied it to images of Fontainebleau sandstones obtained at the NSLS Synchrotron [181]. This software, called 3DMA, underwent a great deal of development over the next decade [182,190] and was made publicly available which enabled it to be used in studies by numerous other authors. The 3DMA software also incorporates indicator kriging segmentation, as described in Section 5.1. Independently, Vogel and Roth developed network extraction techniques based on skeletonization and used them in the characterization of soil data obtained by serial thin sections [183,212]. Meanwhile, a

morphological method that essentially mimics the watershed transform (discussed in Section 5) was introduced by Baldwin [213] and soon developed by others. The method of maximal balls, developed by Silin [214], was also quickly implemented by other groups.

Since this time many methods for partitioning and network extraction have been proposed, often combining elements from one another. These methods are invariably based on either the medial axis transform [181,184,185,187,215], the watershed transform [171–173,213,216] or a maximal ball analysis [186,217–220]. With all these methods, pre- or post-processing is essential to remove excess pores and throats. For skeletonization methods this usually means pruning the skeleton, while for watershed and maximal ball methods it usually involves merging adjacent regions. The principal difference between these methods is that the medial axis approaches try to extract a network with the same topology as the original structure, whereas the other approaches, which use morphological rather than topological information, focus on identifying geometrical constrictions as locations of the pore throats. There have been several studies comparing these methods [220–222], which have showed relatively insignificant differences. It is now generally accepted that the results of network modeling are less sensitive to the method used for the initial partitioning and more sensitive to how the geometrical properties have been assigned to each pore body and pore throat. The first detailed description of how to assign these attributes was the excellent work of Øren et al. [223], who were working with process-based numerical reconstructions of granular samples rather than tomographic images. This work still represents something of a benchmark and although more sophisticated models have been developed for integrating geometry into the network model [215,224,225], there remain major challenges. While there has also been a significant effort in characterizing single- and two-phase flow through throats (see e.g. Patzek [226,227]), little progress has been made in parameterizing the connectivity of crevices in which wetting menisci reside or in relating geometry to imbibition pressure thresholds. These problems are particularly severe when considering mixed-wet systems or three-phase flow.

Another, more fundamental problem of pore-network extraction methods lies in the fact that because they reduce the pore space to a line skeleton, they are unable to capture the geometry of sheet like pores, such as fractures. The morphological methods, as opposed to the skeletonization methods, perform generally better in fractured materials, since they are able to decompose a single fracture into a network of pores and throats. Nevertheless, this is also unsatisfactory; the correct approach is to build pore-space representations that include 2D features, analogous to the medial surface. This is theoretically appealing but presents practical obstacles both for constructing these objects and for the subsequent modeling. Some recent progress in the construction of more sophisticated skeletons suggests that they may soon be suitable as input to pore-network models [155–157].

With the ever increasing size of MCT images, efficiency and scalability of network extraction algorithms is a major concern. Sheppard [173] developed a scalable parallel algorithm for network extraction, capable of analyzing 2048^3 datasets on large cluster-style computers.

The abovementioned network extraction articles give good examples of the applications of this approach in the characterization of pore structure. Two other interesting examples are provided here. Peth et al. [188] imaged grassland and tilled soils using the German DESY synchrotron, then extracted a representative pore network using the 3DMA software [182]. This geometric analysis clearly showed grassland soil having a more open and heterogeneous pore network structure, with more work needed to link pore-space geometry to soil function. Promentilla [228] also used

3DMA in the analysis of cracks in concrete after multiple freeze/thaw cycles and found that cracking appeared earlier and was more severe when insufficient void space was present. A similar analysis could be applied to geomaterials undergoing freeze/thaw cycles.

6.2. Multi-phase flow

In the following, we use the term "multi-phase" flow in reference to all applications involving wetting and nonwetting fluid phases in porous media, i.e., two-phase fluid systems such as air-water, oil-water, supercritical CO_2-brine, and three-phase systems such as air-water-oil, and supercritical CO_2-brine-oil. This implies that we cover applications in a wide range of topics of relevance to water resources: hydrology, environmental science and engineering, petroleum engineering, as well as soil science.

Soon after computed tomography (CT) became commercially available in 1972, researchers in petroleum engineering and soil science started using the technique to solve multi-phase flow problems in their respective fields. Some of the first work was published in the soil science field between 1982 and 1988: e.g. [229–232] who used medical CT scanners to rapidly determine soil bulk density; to map temporal changes in spatial soil moisture distribution; and to track an invading moisture front in three dimensions in a soil sample. Almost simultaneously, namely in 1984, Wang et al. [233] published the first research in the petroleum engineering field where CT was used to map oil saturation distribution in a Berea sandstone core. Shortly after followed a number of similar studies by Wellington and Vinegar and by Hunt et al. [234,235], and the first fairly quantitative study came in 1987 when Vinegar and Wellington [236] used CT to study three-phase flow experiments, and implemented the use of multiple dopants to separate the different fluid saturations. This was followed by Withjack [237] in 1988 who used CT to measure the saturation needed to establish relative permeability curves for Berea sandstone and dolomite cores.

Because all these investigations were carried out with medical CT scanners, resolution was limited to hundreds of micrometers to millimeters and pore-scale resolution, i.e., the ability to image individual grains, pores, and fluid–fluid interfaces, was not feasible. Since then a multitude of these "macro-scale" type studies (where slice averages of the variable of interest is obtained) have been carried out in different geoscience fields and have provided a wealth of information about phenomena and processes at that scale.

Over the years, lab-scale systems with increasingly higher resolutions were developed. As mentioned previously, the first computed _micro_tomography (MCT) system was built by Elliott in the early 1980s at the cost of prohibitively long scan times. In the late 1980s, the resolution drastically increased as microtomography stations were built at synchrotron beam-lines.

As also discussed earlier, lab-scale X-ray systems had also seen sufficient development by the early 1990s that microtomographic imaging could be accomplished more rapidly. Jasti et al. [238] used such a system to produce perhaps the first truly pore-scale images of porous media (e.g. glass beads, Berea sandstone) and fluid distributions of oil and water. In 2000, Clausnitzer and Hopmans [239] took a step further and performed a quantitative study of pore-scale solute breakthrough in sand packs. However, they concluded that to acquire truly pore-scale measurements, synchrotron sources were needed. Since then, laboratory and industrial type MCT has evolved rapidly, and is now on par with synchrotron-based systems in terms of spatial resolution and image quality, although, scan times still are significantly longer for lab-scale systems.

The new developments were quickly implemented for the study of multi-phase flow in porous media. The first studies were focused

on imaging the pore space of consolidated rock (Berea and Fontainebleau sandstones), e.g. [160,205,240,241] who all used microtomography to extract high-resolution three-dimensional information about pore network morphology and connectivity characteristics for subsequent use with pore-scale numerical simulators (see Section 6.1 for more info). To our knowledge, the first multi-phase, and truly pore-scale images were generated by Coles et al. [242] in 1998 using the NSLS tomography facility. Three-dimensional oil and water distributions were measured after oil was displaced by water in a sandstone core plug. Individual sand grains and fluid-filled pores could be identified and the resulting images were used for qualitative comparison to both a lattice-Boltzmann simulator and a pore network simulation.

In the following we provide an overview of some of the different types of multi-phase flow-focused, pore-scale research that has been accomplished using X-ray tomographic imaging in the little more than a decade since these first developments. Recent detailed reviews that are not restricted to pore-scale investigations are provided by Werth et al. [243] with respect to applications in contaminant hydrogeology research; by Taina et al. [244] with respect to applications in soil science; and in hydrology by Wildenschild et al. [15]. As mentioned previously, the focus in the following overview is on pore-scale resolution of features and processes, predominantly pertaining to multi-phase systems.

6.2.1. Two-phase fluid systems

Relatively soon after the first multi-phase images were collected by Coles et al. [242], this capability was implemented to investigate a variety of two-phase flow-related problems.

6.2.1.1. Flow and fluid distribution. The ability to accurately measure fluid distributions and saturations at steady-state or static points during immiscible displacement, drainage/imbibition, or relative permeability measurements was a great step forward in many areas of research. As mentioned previously, Clausnitzer and Hopmans [239] felt that their pore-scale results could be improved on potentially via use of a synchrotron source. In 2002, Wildenschild et al. [15] compared linear attenuation profiles for dry and wet sand samples obtained with synchrotron-based MCT (from the APS GSECARS facility) at two different resolutions (17.1 and 6.7 µm) and found that the resulting images clearly displayed saturation differences in the vertical profile for both resolutions. The higher resolution obviously allowed for more finely resolved analysis, but the authors emphasized the potential REV issues brought about by the higher resolution and thus smaller sample volume analyzed.

In the petroleum realm the Lindquist group at Stony Brook University had acquired some of the first multi-phase images from the NSLS beam-line and used the acquired data to investigate the impact of gels on permeability reduction for both oil-wet and water-wet systems [125,190,245]. Much of their analysis was facilitated by the software developed by the group (3DMA), which (as mentioned previously) allows for detailed network characterization using a medial axis approach [181,182,189].

Meanwhile, researchers at the Australian National University had built a sophisticated MCT system [49] that provided image quality on par with these synchrotron systems, and Turner et al. [246] used this system to image multiple fluid phases during drainage experiments in acrylic bead packs and a Berea sandstone core. The images were of sufficient quality to observe individual pores and fluid interfaces, and the authors were able to report that the residual (trapped) wetting phase could be observed as pendular rings, bridges between adjacent grains, and lenses within pore throats in the sintered glass bead pack.

The effect of fluid drainage rate on residual wetting phase saturation was investigated by Wildenschild et al. [247] who carried out a set of quantitative analyses on synchrotron-based MCT data. The study included sensitivity analyses on the chosen threshold values, and a nearest neighbor analysis on the effect of drainage rate. Residual nonwetting phase distributions was also the focus of the quantitative study by Al-Raoush and Willson [248] and by Schnaar and Brusseau [249]. Their findings are discussed under residual phase morphology below.

The data sets generated by Culligan et al. [91,250] were designed to measure capillary pressure (P_c)-saturation (S_w)-interfacial area (a_{nw}) data, and not specifically to investigate fluid distributions, however these data sets were subsequently used by [251] and [252] to compare P_c–S_w curves and fluid distributions, respectively, obtained with lattice-Boltzmann simulations (based on the actual pore geometry from the images). Porter et al. found surprisingly good agreement between the actual fluid distributions and those simulated using the LB code [252].

The pore scale fluid distribution, the fluid/fluid and fluid/solid interfaces as well as their evolution at different points on the capillary pressure–saturation curve (drainage and imbibition) were studied by Youssef et al. [253]. They performed MCT measurements on 6-mm diameter and 7-mm long Fontainebleau sandstone with 22% porosity, at 5 and 10 µm voxel sizes. Preliminary results on the effect of interfacial tension on the trapping configuration showed local differences in blob connectivity and local saturation. They also compared the developed water/oil interfaces between imbibition and drainage conditions at equal saturation and found significant differences that they suggested can explain the hysteresis observed in the relative permeability and P_c–S curves.

As discussed in Section 4, Silin et al. [81] reported some of the first high-pressure experiments where a rock sample was saturated with water and supercritical CO_2. However, Silin et al. [81] reported that the quality of the images was far from perfect: it captured only major features of the pores, but entirely missed the small pores and crevices. Nevertheless, the authors reported that the major features were sufficient for modeling the distribution of the non-wetting fluid with the method of maximal inscribed spheres [217]. As also mentioned in Section 4, Iglauer et al. [82] very recently reported on successful supercritical CO_2-brine imaging experiments where they were able to measure trapped CO_2 amounts and cluster sizes. They were also able to confirm the hypothesis that supercritical CO_2 will act as the non-wetting phase in the Doddington sandstone that was investigated, yet, they found that trapping was less efficient for supercritical CO_2, than observed for an analogue fluid (n-octane), indicating an increased water contact angle for the sandstone at high pressure.

6.2.1.2. Residual phase morphology. As illustrated in Fig. 13, characterization has come a long way since Chatzis et al. "imaged" residual nonwetting phase blob structure and size using polymerized styrene. This creative approach involved trapping styrene (as the nonwetting phase) in the pore space and then heating the styrene to 80 °C for 48 h to solidify the styrene. The styrene was then leached with a series of mineral acids to produce an object such as the example shown in Fig. 13. Obviously, imaging of residual phase morphology is now much less cumbersome as MCT can produce fully three-dimensional data in a very short amount of time.

Residual nonwetting phase blob morphology and their statistical quantities in oil-wet glass beads (imaged at 12.5 µm) was specifically studied by Al-Raoush and Willson [248], who measured properties such as blob volume, interfacial area, and sphericity of the trapped nonwetting phase. These authors also investigated potential relationships between pore network architecture and nonwetting phase morphology, and as expected, found that the nonwetting phase was trapped primarily in the largest pores, as well as the pores with the highest aspect ratios and coordination numbers. Similar work was carried out by Schnaar and Brusseau
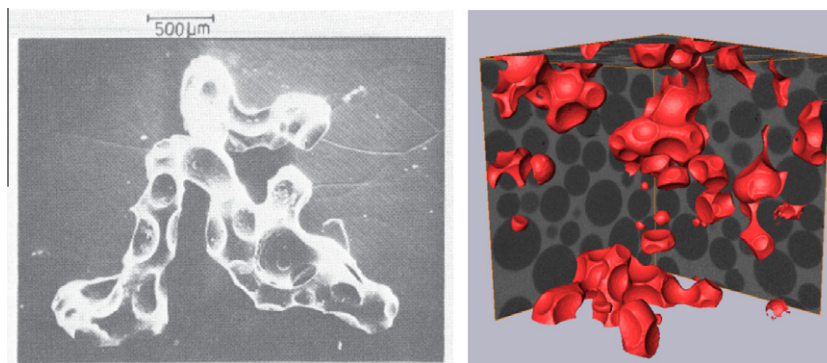
Fig. 13. (Left) image of polymerized styrene blob in a glass bead pack from Chatzis et al. [4] with permission. Image "acquisition" took 48 h and the result was a physical 3D object. (Right) similar geometry captured with synchrotron-based MCT in 5 minutes, producing a digital data set to be used for further quantitative analysis.

[249] for natural sands and soils, by Prodanović et al. [190] for oil-wet polyethylene cores, and on sandstone cores by Prodanovic et al. [125]. Iglauer et al. [167] also studied residual trapping in sandstone cores (imaged at 9 μm) and found that most of the residual nonwetting phase occupied large clusters and also covered multiple pores. They pointed out the advantage of the variety in cluster sizes, which implies that a significant surface area would be available for geochemical reaction and dissolution for instance during carbon dioxide storage in aquifers. Comparable results were also found by Youssef et al. [254] who performed similar analyses for glass bead packs at a resolution of 25–30 μm. In addition, they found that the majority of the oil blobs were larger than the average pore size and that the mean oil blob size was approximately five times larger than the average pore.

The effect of texture of the porous medium was investigated by Schnaar and Brusseau [249]. They analyzed blob morphologies for three different porous media, comprising a range of particle-size distributions, and found – in accordance with the above studies – that the majority of blob surface area and volume was observed for the largest blobs, but also that the ratio of median blob size to median grain size was close to unity for the textures analyzed. Following their work on characterizing blob morphology, Schnaar and Brusseau [255] used synchrotron-based MCT to characterize pore-scale dissolution of NAPL trapped in natural sandy porous media, and used similar approaches to their earlier studies to describe the resulting change in blob morphology that took place during dissolution.

The effect of wettability on blob morphology was studied by Karpyn et al. [256] and is discussed below under wettability effects. Kumar et al. [257] studied the effect of trapped residual hydrocarbon saturation as a function of the initial water saturation, the flooding rate, and the wettability to oil and water. The imbibition experiments were carried out on a number of sandstone and reservoir carbonate samples of varying complexity. In general, agreement was found between the tomography-based trends and those reported in literature for the water-wet samples, i.e., a decrease in residual oil phase saturation was observed with increasing capillary number, and a similar trend was found for a mixed-wet core.

The effects of successive freeze-thaw cycles on the pore-scale NAPL spatial distribution, ganglia morphology, and availability for dissolution – and hence on contaminant fate and transport – were investigated in a new study by Singh et al. [258]. Experiments were performed in a glass bead pack, using a mixture of dodecane and iodononane as the NAPL. Based on the findings of this study, two mechanisms for NAPL mobilization and rupture during freeze-thaw were proposed: a freezing-induced expulsion mechanism and a freezing-induced cutoff mechanism, both caused by the expansion of water during freezing. The study has significant implications for the effect of freeze-thaw cycles on surface NAPL spills in cold regions, and for the behavior of hydrocarbon–water–ice systems on Earth and other planets.

In addition to the ability to characterize overall residual phase morphology, MCT has recently also been shown to allow for quantification of phase connectivity. Porter et al. [92] was able to distinguish bulk wetting phase from disconnected wetting phase in a glass bead pack, and found that even at very low saturations ($S_w = 0.09$) the wetting phase was relatively well-connected throughout the sample. Similarly, Armstrong and Wildenschild [259] was able to separate connected and disconnected wetting and nonwetting phase to allow for comparison of curvature estimates based on the MCT images, to curvatures (capillary pressure) measured externally using a pressure transducer, see Fig. 8(v) and (vi) for example images.

6.2.1.3. Fluid–fluid interfacial characteristics. The innovation with respect to optics and instrumentation at synchrotron tomography beam-lines has facilitated generation of data of sufficient quality to extract ever more detail from the images. The first MCT-based measurements of fluid–fluid interfacial area were published by [91] in 2004. They measured the complete P_c–S_w–a_{nw} relationship for the air–water fluid system in a glass bead pack at 17 μm resolution. The results showed that the fluid–fluid interfacial area increased as saturation decreased at high saturations, until a maximum was reached at 20–35% saturation, where after the area decreased as the saturation continued to zero. The findings supported results of numerical studies reported in the literature [194,260,261]. The data set was subsequently used in combination with lattice-Boltzmann-generated data to investigate the uniqueness of the P_c–S_w–a_{nw} relationship and it was found that the relationship supports the theory of [262,263].

Culligan et al. [250] and Porter et al. [92] carried out similar measurements for a NAPL–water–glass bead system. The focus of the work of this group has been on the capillary-dominated wetting–nonwetting phase interfacial areas and simultaneous measurements of capillary pressure, saturations, and interfacial areas, whereas [249,264–269] have focused more on measurements of the total wetting–nonwetting phase interfacial areas and the comparison to measurements made with gas or liquid phase partitioning interfacial tracers. While the tracer-based method provides an estimate of effective *total* (capillary and film) interfacial area, MCT can be used to determine both capillary-associated and total interfacial areas. In their 2006 comparison study Brusseau's group [265] found significantly higher areas with the tracer test method

than when they were measured with MCT. They suggested that this result may be caused by the lack of resolution in MCT and thus that interfacial area associated with films and surface roughness cannot be accurately represented using MCT. As a consequence, [265] concluded that the gas phase tracer method has advantages over MCT when it comes to characterization of *total* wetting-nonwetting interfacial areas. However, when interfacial areas associated with specific domains is of interest (such as capillary-associated interfacial area), MCT might prove more useful than the tracer-based methods. In recent work, the surface roughness hypothesis was verified for a smooth glass bead system by Narter and Brusseau [267] in that interfacial areas were essentially identical based on the two methods in the absence of surface roughness.

Costanza-Robinson et al. [269] measured total air–water interfacial areas for nine natural and model sandy porous media as a function of water saturation using synchrotron-based MCT. They found that maximum interfacial area compared favorably to the media geometric surface areas. Importantly, relative interfacial area (i.e., normalized by geometric surface area) versus water saturation plots for all media collapsed into a single linear cluster suggesting that geometric surface area is an important, and perhaps sufficient, descriptor of sandy media that governs total smooth interfacial area–water saturation relationships. Measured relationships were used to develop an empirical model for estimating interfacial area–water saturation relationships for sandy porous media.

In a very new study, Costanza-Robinson et al. [270] address the issue of representative elementary volume (REV) for tomography analysis, which has become a criterion for demonstrating the quality of MCT measurements in porous media systems. In this work, deterministic REVs for porosity, saturation, and air–water interfacial area were estimated using a set of 49 MCT images of eight unsaturated homogeneous porous media with saturation heterogeneity present in varying degree. They suggested that because their results showed that achieving porosity REV was largely sufficient for ensuring reliable data (a condition that is readily achieved for typical MCT image sizes according to their study) it may be possible to extract numerous volume averaged measurements for various system variables from multiple windows of each image. Boundary conditions might even be chosen specifically to introduce macroscopic heterogeneity in system conditions (e.g., a large gradient in fluid saturation) with the intent of gathering a greater range of information from a single image. This approach would be particularly useful for delineating nonlinear relationships between system variables, such as the parabolic relationship observed for capillary-dominated interfacial areas and wetting phase saturation [91,92,250,265] using many fewer images. Moreover, because REV for porosity is relatively small, subject to porous media packing constraints, Costanza-Robinson et al. suggest that even smaller sample sizes than those currently used may yield reliable information. Use of smaller samples would facilitate higher spatial resolution and the ability to delineate and quantify even smaller features in the images.

As mentioned in Section 5, Armstrong et al. [13] have recently compared P_c measured with external pressure transducers to P_c calculated from interfacial curvature in MCT images for glass bead systems. The potential to measure P_c from image curvature presents an exciting opportunity for understanding variations in fluid–fluid pressures, saturations, and interfacial areas for both two-phase and three-phase fluid systems, where the various inter-phase pressures cannot be measured with equipment external to the system.

6.2.1.4. Wettability effects. To our knowledge, the first pore-scale tomography-based study involving wettability was reported by

Han et al. [271] who carried out experiments to investigate the effect of wettability on the retention and transport of viruses in porous media. To address this they packed two columns with glass beads that were either water-wet (100% hydrophilic) or fractionally-wet (50% hydrophilic and 50% hydrophobic), and imaged them with MCT at 11 µm. Analysis of the microtomography images indicated that the number of blobs in the fractionally-wet medium was four times less than in the water-wet medium of the same volume. The configuration of water in the hydrophilic glass beads facilitated closer contact between the viruses and the interfaces (i.e., solid–water and air–water interfaces), resulting in increased virus retention, whereas flow bypassed water-repellent regions in fractionally-wet beads, making a fraction of favorable attachment sites inaccessible to the virus particles. Therefore, transport of viruses through the unsaturated fractionally-wet medium was greatly enhanced.

Kumar et al. [272] presented results for drainage and imbibition in Fontainebleau sandstone, sucrosic dolomite, and oomoldic grainstone cores at well defined wettability states using air and water. Kumar found that the image-based residual gas saturations and water saturations were in good quantitative agreement with the values obtained via other methods. The impact of wettability on the pore-scale characteristics of residual nonaqueous phase liquids (NAPLs) was explored by Al-Raoush [256]. Four systems comprised of 0%, 25%, 50%, and 100% NAPL-wet (silane-treated sand grains) mass fractions were imaged and analyzed for residual NAPL. They reported a significant impact of spatial variation in the porous media surface wettability on the pore-scale architecture of residual NAPL: due to trapping in large pore bodies, the residual NAPL blob size and length increased as the fraction of water-wet surfaces increased. Landry et al. [273] also studied the effect of wettability on fluid distributions, blob characteristics, and surface and interfacial areas, but covered a wider range of saturations during drainage and imbibition in glass beads. The results showed that the differences in wetting characteristics were clearly reflected in the blob populations. The number of blobs in the oil-wet porous medium was three times greater than that of the water-wet porous medium at similar saturations; they suggested that the increase in blob number resulted from the increase in the number of smaller blobs inhabiting the smaller pore spaces.

In a very recent study, Armstrong and Wildenschild [259] used MCT to study the effect of wettability on microbial enhanced oil recovery (MEOR) using two different microbial species. They imaged 0%, 25%, and 50% oil-wet columns after water flooding, and after MEOR. Results indicate that the larger residual oil blobs and residual oil held under relatively low capillary pressures were the main fractions recovered during MEOR. Residual oil saturation, interfacial curvatures, and oil blob sizes were measured from the MCT images and used to develop a conceptual model for MEOR in fractional-wet systems. Overall, results indicate that MEOR was effective at recovering oil from fractional-wet systems with reported additional oil recovered (AOR) values between 44% and 80%; the highest AOR values were observed in the most strongly oil-wet system.

6.2.1.5. Soil aggregates and fluid flow. As tomography capabilities have increased, especially in terms of resolution, more and more detailed studies have also been undertaken to address open question in soil science/soil physics.

Carminati et al. [274] and Kaestner et al. [275] used the SLS TOMCAT beam-line to image two soil aggregates placed in close contact on top of each other at 5.9 µm resolution. Water was imbibed from below. In the images, the water distribution between the two aggregates was clearly visible. The authors found that the larger pores in the contact region were rapidly drained because of aggregate surface roughness and the water potential decreased

as a result. Similarly, Tippkötter [276] used microfocus CT to visualize both soil matrix and soil water in natural soil aggregates, and were also able to resolve films and estimate film thicknesses (at 3 and 10.6 μm respectively for the two soils). The authors did point out that although water films in pores were clearly detectable, open questions still remain, especially with respect to the thickness of the water films.

On a slightly larger scale, a significant body of work exists, and research is on-going, in the area of macropore flow and transport. However, because macropores (earthworm channels, roots, cracks, and fissures in soils) are much larger features and therefore generally analyzed at much larger scale and often with medical CT scanners, further review is not provided here, we refer to [244] and [33].

6.2.2. Three-phase fluid systems

To our knowledge, there are only a few existing publications reporting pore-scale studies of three-phase flow in porous media. The first was published by Alvarado et al. [277] and reported on three-phase investigations using an industrial micro-focus CT. Samples of quartz sand with an average grain diameter of approximately 1 mm were packed in 7-mm inside diameter and 120 mm long core holders and imaged at 9 μm voxel resolution. Three fluids (water, benzyl alcohol, and decane) were imaged in the pore space, and the data was sufficient to resolve all three phases, yet thin wetting layers could not be detected. The study showed the potential of using MCT to study three phase-fluid systems.

Schnaar and Brusseau [268] used synchrotron-based MCT to generate images at 10.9 μm of a NAPL (tetrachloroethene) residing in three natural, sandy porous media for both a three-phase situation (water–air–NAPL) and a two-phase situation (water–NAPL) systems. NAPL was to a certain extent configured as lenses and films between the air and water phases, a geometry that would obviously not be observed in the two-phase system. The blob size distributions were skewed towards smaller size and larger variance for the three-phase systems as compared to the two-phase systems. In addition, the presence of the NAPL lenses and films resulted in larger specific surface areas in the three-phase systems. Similar results were obtained by Brown et al. [278] who imaged three-phase fluids in a sintered glass bead core at similar resolution (11.3 μm), but because they imaged much larger pores (in a glass bead pack), they were able to resolve the three phases in even more detail. They also observed that when oil first contacted the trapped air bubbles during drainage, a film of oil (the intermediate phase) coated the air phase. This process is generally referred to as film spreading and at this point the air–water interfacial area became negligible, and the air–water interfacial contact was never reestablished.

6.3. Water-related biofilms/soil microbiology

Only limited work has been carried out using MCT in the realm of biofilm and soil microbial characterization. This is a natural consequence of biofilms and microbes having a very low X-ray cross section. Also, once situated inside a porous medium and thus requiring X-rays of significant energy for penetration, the biological phase becomes almost invisible.

Nunan et al. [279] investigated microbial micro-habitat structure using MCT, but from the angle of characterizing the pore geometry, not in terms of imaging biofilms or the soil microbiology. Thieme [280] used microscopic tomography (beam-line 6.3 at the ALS) based on zone-plate technology and soft X-rays to visualize flocs of colloidal soil particles and associated bacteria at sub-100 nm resolution. However, only recently (2011) has MCT been implemented for imaging and quantifying variables related to the presence of biofilms *inside* porous media. Davit et al. and Iltis

et al. [10,11] used synchrotron-based MCT and lab MCT to image intact biofilms inside porous media, see examples in Fig. 8(iii). The two studies were based on use of different contrast agents to enhance the contrast of the biofilms to X-rays. Davit et al. [10] used a $BaSO_4$ suspension to separate biofilms from the aqueous phase and solid pore geometry, while Iltis et al. [11] used silver-coated spheres that attach to the outer surface of the biofilm to obtain the biofilm geometry. Both studies illustrated the potential for studying the effects of biofilm growth, clogging, nutrient pathway alteration, etc. at the pore-scale, but also addressed limitations of the techniques such as the effect of radiation dose on microbial growth.

6.4. Reactive transport

Altman et al. [281] evaluated synchrotron-based MCT for visualizing transport processes in low-porosity materials. They used Cs and I as tracers and based on their results concluded that under the right circumstances, MCT can be used to visualize transport of these tracers. Among the limitations reported, were the range in concentration data needed, that pore sizes needed to exceed 2–50 μm (depending on the sample size and system setup), that an REV can be contained by a 2–10 mm diameter sample (implying a fine pore size), and that significant changes do not occur within the 25–50 min needed to collect data (slow transport). As the authors proposed, the time constraint has decreased drastically since this work was published in 2005 (the acquisition time is now on the order of 5 min).

Reactive flow induced pore structure changes in Hanford sediment was studied using synchrotron-based MCT at the NSLS by Cai et al. [282]. They were able to quantify dissolution and secondary precipitation in the sediments exposed to simulated caustic waste. A net reduction in porosity and in pore sizes $< 10^{-4}$ mm^3 in volume, and in the number of throats, as well as an increase in the number of pores of larger size were observed. A natural consequence of the reduction in number of throats was a decreased coordination number for pores of all sizes. It was consistently found that dissolution was prevalent in the larger pores, precipitation took place in smaller pores, and small throats were clogged.

An example showing differences between images captured before and after CO_2-induced dissolution is included in Fig. 8(iv). As the figure illustrates, dissolved rock and CO_2-induced areas of increased microporosity can be clearly identified and quantified using MCT imaging.

In the geological CO_2 sequestration realm, Noiriel et al. [283] published the first quantitative results from a percolation experiment of a structurally heterogeneous limestone rock. Modeling reactive transport in porous media relies on adequate characterization of reactive surface area and permeability as well as changes in these properties that may result from precipitation and dissolution. In the study by Noiriel et al. [283] the processes accompanying flow of CO_2-enriched water in a limestone core over approximately 24 h were constrained by chemical measurements (pH, P_{CO_2}, Ca concentration) at the inlet and outlet of the core, and permeability was measured throughout the experiment. The samples were imaged at 4.9 μm resolution at beam-line ID19 at the ESRF. Particle removal observed in the cores was associated with a large increase in permeability in the early stage of the experiment, whereas porosity remained quasi-constant over the same time; only a low fraction of the pore space (and thus, of the fluid-rock interface) was involved in this process. During later stages of dissolution, permeability increased via reduction of pore wall roughness and also due to increasing pore path connectivity.

Since this first study focusing on CO_2 injection, a number of studies using MCT imaging have investigated geochemical transformation of rocks by stored carbon dioxide, e.g. [284–287]. In

the most recent study by this group [287] the relationship between dissolution phenomena and the resulting changes in reactive surface area and permeability were explored. A set of dissolution experiments of pure calcite rock samples were conducted and the reactive surface area computed from MCT data obtained before and after dissolution. The results were used to validate a power law empirical model proposed by Luquot and Gouze [285] that relates reactive surface area to porosity.

The proper description of permeability in terms of porosity was also investigated by Armstrong and Ajo-Franklin [288] using synchrotron-based MCT at the Advanced Light Source. Their primary focus was on calcium carbonate biomineralization induced by bacteria in glass bead columns. Porosity changes in the 8-mm i.d. bead pack were observed at 4.5 μm resolution, and a three order of magnitude reduction in permeability was measured over the 60-h timescale of the precipitation experiment. They found that traditional Kozeny–Carman models were inadequate for predicting porosity–permeability relationships observed during precipitation and concluded, in agreement with their French colleagues, that more sophisticated models will be needed to effectively predict changes in transport properties during precipitation and/or dissolution.

6.5. Colloids and particle dynamics

With increasing spatial resolution, it has become feasible to visualize colloids and particles in porous media. The prevalence of colloid deposition at grain-to-grain contacts in two porous media (spherical glass beads and angular quartz sand) was examined by Li et al. [289] using MCT. Colloids were prepared by coating gold on hollow ceramic microspheres (36 μm in size). The colloids were visible in reconstructed images, and analysis showed that a significant fraction of the deposited microspheres were deposited at grain-to-grain contacts in both porous media under the conditions examined. The results also demonstrated that filtration theory captures the essential elements of colloid deposition in the absence of an energy barrier despite a lack of detailed accounting for grain-to-grain contacts. Gaillard et al. [9] similarly used difference MCT (using absorption edge specific imaging) to identify the morphology of colloidal deposits formed in porous media, see Fig. 8(ii). The authors tracked transport of colloidal ZrO_2 particles through an idealized porous medium consisting of glass beads. Their results show that particle deposition was largely controlled by the local pore geometry, and that deposition was fairly heterogeneous throughout the porous medium. In a subsequent study, Chen et al. [290] studied transport and mixing of sand and spherical glass in a laboratory flume. They extracted cores from the streambed at four different times, and the evolution of spatial patterns within the bed was evaluated using MCT. A propagating sediment mixing front was observed that began at the bed surface and the authors suggested that MCT provides a method for advanced characterization of mixing and transport of fine sediments in aquatic systems. Using a similar approach, the same group [291] studied hyporheic exchange flow using colloids. They showed that clogging of flow paths by colloids lead to a decrease in permeability and thus alteration of hyporheic flow paths near the bed surface. Even though the deposition of colloids reduced the average exchange flux, a higher exchange flux was observed in certain locations, because the spatial variability in pore water flow increased.

6.6. Elemental mapping (XRF)

As an early example of the use of X-ray fluorescence (XRF) tomography in a water-related discipline, Hansel et al. [292] studied the deposition of iron and other metals on the roots of mine-waste affected aquatic plants. The goal was to gain a better understanding of how metal is cycled through wetland ecosystems. XRF tomography was used to identify the spatial distribution and chemical environment of Fe, Mn, Pb, and Zn on the roots of a wetland plant. Similarly, Hansel et al. [293] investigated the role of root-borne carbonate nodules in the attenuation of contaminant metals in aquatic plants, and mapped Fe, Pb, Zn and Mn in a 300 μm cross-section of a plant root. The information about the distribution of elements in the interior of roots could not be obtained without XRF because slicing would damage the elemental maps. Similarly, [294,295] studied the arsenic distribution in cattail roots near the Woburn, MA Superfund site using fluorescence tomography. In addition to total arsenic concentrations, they also were able to measure the oxidation states using edge-specific imaging, and thereby map the distribution of As^{3+} and As^{5+} in the roots. Very recently, Mayhew et al. [6] mapped Fe speciation and distribution during fluid-mineral reactions after 48 h and after 10 months. The results provided otherwise unattainable new insights into heterogeneous Fe speciation in complex geological media under highly reducing conditions, as illustrated in Fig. 14. The long data acquisition times have traditionally prohibited the application of XRF to highly hydrated biological samples which suffer both radiation damage and dehydration during extended analysis. However, via careful sample preparation and by taking advantage of recent improvements in fast fluorescence detectors, this problem can be alleviated, allowing for investigation of metal distribution in biological samples that generally tend to be sensitive to the radiation exposure. Lombin et al. [296] were recently able to image the distribution of nickel and zinc in hydrated plant roots, thus demonstrating the increased potential of the technique.

7. Summary

As demonstrated with this review, cutting-edge pore-scale research based on tomographic imaging has matured to a point where rather sophisticated analysis and interpretation is the norm, and it is no longer common to encounter a publication where the
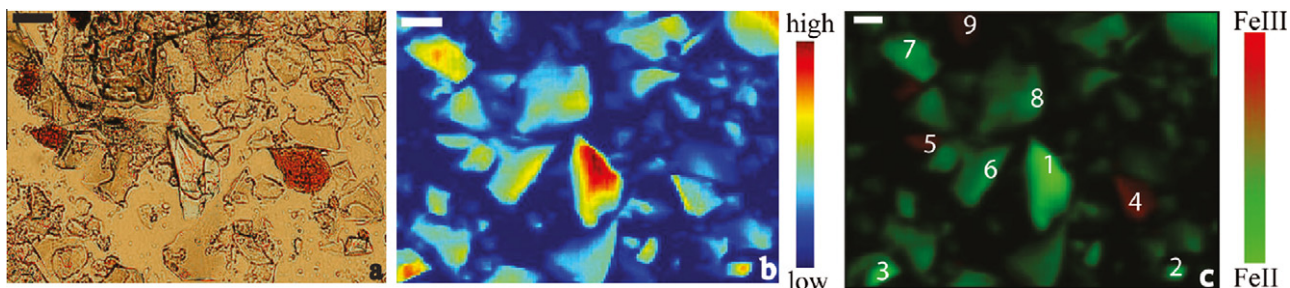

Fig. 14. (a) Plane polarized light photomicrograph of the sample area of interest (10× mag). (b) SR-μXRF total Fe intensity mapped at 11 keV. (c) Distribution of Fe(II) and Fe(III) obtained from XANES fitting the five energy maps. Scale bars = 40 μm. From [6] with permission.

results are presented as a mere qualitative comparison of images – nor is it warranted considering the potential there is for quantitative analysis. Along with developments in technique and equipment, there is now a substantial body of literature supporting quantitative analysis of processes related to the environmental and geosciences fields.

Similarly, the types of objects and processes that can be studied with a non-invasive technique like MCT are expanding all the time. By its very nature, MCT has traditionally excluded dynamic processes, however with recent developments in reconstruction techniques and detector speed, even continuously evolving phenomena can now be imaged and quantified with MCT, and we have only just seen the beginning of this so-called fast tomography effort. Multi-scale imaging systems are being developed to image, and accurately register, samples over scales spanning many orders of magnitude, and to combine MCT with different modalities such as BSEM and FIB-SEM see Fig. 8(i); innovative use of contrast agents allow for imaging of low density materials such as biofilms; and techniques are being developed to measure increasingly minute detail from the images, such as fluid–fluid interfacial areas and curvatures.

In a recent article reviewing non-invasive imaging techniques, Werth et al. [243] stated that "X-ray methods present the highest resolution and flexibility for 3D natural porous media characterization, and 3D characterization of fluid distributions in natural porous media". This is certainly true, and despite the method's limitations in terms of material discrimination, resolution and acquisition time, we are optimistic that the current rapid progress on many fronts will be sustained for many years to come. This is particularly true if the innovative groups of users keep pushing the limits of basic imaging capability, as well as the limits of what types of materials and objects the technique can be applied to.

The tremendous value in the application of MCT to the study of geosciences related phenomena, and particularly fluid flow and related transport in porous media, should be evident. Besides the many advances already gained and reported in the literature in terms of improved understanding of flow and transport phenomena, the other palpable gain has been, and will be, in the validation of pore-scale models, with implications for these phenomena at much larger scales.

Acknowledgements

References

[1] Winick H. Synchrotron Radiation Sources: A Primer. World Scientific Publishing Company, Series on Synchrotron Radiation Techniques; 2010.

[2] Schlachter, A.S., et al. Synchrotron radiation. in AccessScience. ©McGraw-Hill Companies; 2008. <http://www.accessscience.com>.

[3] Myers GR et al. Polychromatic cone-beam phase-contrast tomography. Phys Rev A 2007;76(4):045804.

[4] Chatzis I, Morrow NR, Hau TL. Magnitude and detailed structure of residual oil saturation. SPE J 1983;23(2):10681-PA.

[5] Sheppard A. Techniques for image enhancement and segmentation of tomographic images of porous materials. Physica A 2004;339(1–2):145–51.

[6] Mayhew LE, Webb SM, Templeton AS. Microscale imaging and identification of Fe speciation and distribution during fluid-mineral reactions under highly reducing conditions. Environ Sci Technol 2011;45(10):4468–74.

[7] Varslot TK et al. Combining high-fidelity helical micro-tomography with region-of-interest scanning for improved core characterization. In: 2011 International Symposium of the Society of Core Analysts, Austin, TX, USA; 2011.

[8] Sok RM et al. Pore scale characterization of carbonates at multiple scales: Integration of MicroCT, BSEM and FIBSEM. In: Proceedings of the 2009 international symposium of the society of core analysts, Noordwijk, The Netherlands; 2009.

[9] Gaillard J-F et al. Imaging of colloidal deposits in granular porous media by X-ray difference micro-tomography. Geophys Res Lett 2007;34(18).

[10] Davit Y et al. Imaging biofilm in porous media using X-ray computed microtomography. J Microsc 2011;242(1):15–25.

[11] Iltis GC et al. Imaging biofilm architecture within porous media using synchrotron-based X-ray computed microtomography. Water Resour Res 2011;47(2):1.

[12] Kumar A et al. Micro-petrophysical experiments via tomography and simulation. In: GeoX 10: advances in X-ray tomography for geomaterials. John Wiley & Sons; 2010.

[13] Armstrong RT, Porter ML, Wildenschild D. Linking pore-scale interfacial curvature to column-scale capillary pressure. Adv Water Resour [in press].

[14] McCullough EC. Photon attenuation in computed tomography. Med Phys 1975;2(6):307.

[15] Wildenschild D et al. Using X-ray computed tomography in hydrology: systems, resolutions, and limitations. J Hydrol 2002;267(3–4):285–97.

[16] Herman GT. Correction for beam hardening in computed tomography. Phys Med Biol 1979;24:81.

[17] Ketcham RA, Carlson WD. Acquisition, optimization and interpretation of X-ray computed tomographic imagery: applications to the geosciences. Comput Geosci 2001;27(4):381–400.

[18] Hsieh J et al. An iterative approach to the beam hardening correction in cone beam CT. Med Phys 2000;27:23.

[19] Iassonov P, Tuller M. Application of segmentation for correction of intensity bias in X-ray computed tomography images. Vadose Zone J 2010;9(1):187–91.

[20] Rivers ML, Sutton SR, Eng P. Geoscience applications of X-ray computed microtomography. In: Proceedings of the SPIE conference on developments in X-ray tomography II, Denver, CO; July 1999. p. 78–86.

[21] Arhatari BD et al. Phase contrast radiography: image modeling and optimization. Rev Sci Instrum 2004;75(12):5271–6.

[22] Davis TJ et al. Phase-contrast tomography of weakly absorbing materials using hard X-rays. Nature 1995;373(6515):595–8.

[23] Wilkins SW et al. Phase-contrast imaging using polychromatic hard X-rays. Nature 1996;384(6607):335–8.

[24] Gureyev TE et al. Refracting Rontgen's rays: propagation-based X-ray phase contrast for biomedical imaging. J Appl Phys 2009;105(10).

[25] Cloetens P et al. Holotomography: quantitative phase tomography with micrometer resolution using hard synchrotron radiation x rays. Appl Phys Lett 1999;75(19):2912–4.

[26] Pfeiffer F et al. Phase retrieval and differential phase-contrast imaging with low-brilliance X-ray sources. Nat Phys 2006;2(4):258–61.

[27] Nugent KA. Coherent methods in the X-ray sciences. Adv Phys 2010;59(1):1–99.

[28] Myers GR et al. Polychromatic cone-beam phase-contrast tomography. Phys Rev A 2007;76(4).

[29] Burvall A et al. Phase retrieval in X-ray phase-contrast imaging suitable for tomography. Opt Exp 2011;19(11):10359–76.

[30] Yang YS et al. Feasibility of a data-constrained prediction of hydrocarbon reservoir sandstone microstructures. Meas Sci Technol 2010;21(4).

[31] Kinney JH, Nichols MC. X-ray tomographic microscopy (XTM) using synchrotron radiation. Annu Rev Mater Sci 1992;22(1):121–52.

[32] Boisseau P. Determination of three dimensional trace element distributions by the use of monochromatic X-ray microbeams, Ph.D. Thesis. MIT; 1986.

[33] Lombi E, Susini J. Synchrotron-based techniques for plant and soil science. Opportunities, challenges and future perspectives. Plant Soil 2009;320(1–2):1–35.

[34] Hounsfield GN. Computed transverse axial scanning (tomography). I. Description of system. Br J Radiol 1973;46:1016.

[35] Sato T et al. X-ray tomography for microstructural objects. Appl Opt 1981;20(22):3880–3.

[36] Elliott JC, Dover SD. X-ray microtomography. J Microsc 1982;126(Pt 2):211.

[37] Elliott JC, Dover SD. X-ray microscopy using computerized axial tomography. J Micros. 1985;138(June):329–31.

[38] Fontijn LA, Peugeot RS. An operational 150 kV microfocus rod anode X-ray system for non-destructive testing. NDT Int 1978;11(5):229–32.

[39] Aoki S, Sakayanagi Y. A high-brilliance microfocus x-ray source with an LaB^6 cathode. Jpn J Appl Phys 1981;20(12):2419–20.

[40] Burstein P et al. The largest and smallest X-ray computed tomography systems. Nucl Instrum Methods Phys Res Sect A – Accelerators Spectrometers Detectors Assoc Equipment 1984;221(1):207–12.

[41] Seguin FH et al. X-ray computed tomography with 50 μm resolution. Appl Opt 1985;24(23):4117–23.

[42] Bateman JE et al. Digital X-ray microscopy with a microfocal X-ray generator and an MWPC area detector. Nucl Instrum Methods Phys Res Sect A – Accelerators Spectrometers Detectors Assoc Equipment 1988;273(2–3):767–72.

[43] Flannery BP et al. Three-dimensional X-ray microtomography. Science 1987;237(4821):1439.

[44] Holdsworth DW, Drangova M, Fenster A. A high-resolution XRII-based quantitative volume CT scanner. Med Phys 1993;20:449.

[45] Morton EJ et al. 3-Dimensional X-ray microtomography for medical and biological applications. Phys Med Biol 1990;35(7):805–20.

[46] Machin K, Webb S. Cone-beam X-ray microtomography of small specimens. Phys Med Biol 1994;39(10):1639–57.

[47] Sasov A, Van Dyck D. Desktop X-ray microscopy and microtomography. J Microsc 1998;191(2):151–8.

[48] Davis GR, Elliott JC. X-ray microtomography scanner using time-delay integration for elimination of ring artefacts in the reconstructed image. Nucl Instrum Methods Phys Res Sect A – Accelerators Spectrometers Detectors Assoc Equipment 1997;394(1–2):157–62.

[49] Sakellariou A. X-ray tomography for mesoscale physics applications. Physica A 2004;339(1–2):152–8.

[50] Withers PJ. X-ray nanotomography. Mater Today 2007;10(12):26–34.

[51] Mayo S et al. X-ray phase-contrast microscopy and microtomography. Opt Exp 2003;11(19):2289–302.

[52] Varslot T et al. Fast high-resolution micro-CT with exact reconstruction methods. In Stock SR, editor. Developments in X-ray tomography Vii; 2010.

[53] Tkachuk A et al. X-ray computed tomography in Zernike phase contrast mode at 8 keV with 50-nm resolution using Cu rotating anode X-ray source. Z. Kristallographie 2007;222(11/2007):650–5.

[54] Izzo JR et al. Nondestructive reconstruction and analysis of SOFC anodes using X-ray computed tomography at sub-50 nm resolution. J Electrochem Soc 2008;155(5):B504–8.

[55] Robinson AL. History of synchrotron radiation. X-ray Data Booklet, section 2.2. (LBNL/PUB-490 Rev. 2); 2001.

[56] Sham TK, Rivers ML. A brief overview of synchrotron radiation. Appl Synchrotron Radiat Low-Temp Geochem Environ Sci 2002;49:117–47.

[57] Borodin YI et al. Scanning X-ray difference microscopy and microtomography using synchrotron radiation of the storage ring VEPP-4. Nucl Instrum Methods Phys Res Sect A 1986;246(1–3):649–54.

[58] Bonse U et al. High resolution tomography with chemical specificity. Nucl Instrum Methods Phys Res Sect A 1986;246(1–3):644–8.

[59] Spanne P, Rivers M. Computerized microtomography using synchrotron radiation from the NSLS. Nucl Instrum Methods Phys Res Sect B 1987;24–25:1063–7.

[60] D'Amico KL et al. X-ray microtomography with monochromatic synchrotron radiation (invited). Rev Sci Instrum 1989;60(7):1524.

[61] Takeuchi A et al. Submicrometer-resolution three-dimensional imaging with hard X-ray imaging microtomography. Rev Sci Instrum 2002;73(12):4246–9.

[62] Herman GT, Lakshminarayanan AV, Naparstek A. Convolution reconstruction techniques for divergent beams. Comput Biol Med 1976;6(4):259–62.

[63] Feldkamp LA, Davis LC, Kress JW. Practical cone-beam algorithm. J Opt Soc Am A 1984;1:612–9.

[64] Xu F, Mueller K. Accelerating popular tomographic reconstruction algorithms on commodity PC graphics hardware. IEEE Trans Nucl Sci 2005;52(3):654–63.

[65] Natterer F. The mathematics of computerized tomography. SIAM, Society for Industrial and Applied Mathematics; 2001.

[66] Myers GR et al. Dynamic tomography with a priori information. Appl Opt 2011;50(20):3685–90.

[67] Ballabriga R et al. Medipix3: a 64 k pixel detector readout chip working in single photon counting mode with improved spectrometric performance. Nucle Instrum Methods Phys Res Sect A – Accelerators Spectrometers Detectors and Associated Equipment 2011; 633:15–8.

[68] Gimenez EN et al. Characterization of Medipix3 with synchrotron radiation. IEEE Trans Nucl Sci 2011;58(1):323–32.

[69] Kraft P et al. Characterization and Calibration of PILATUS detectors. IEEE Trans Nucl Sci 2009;56(3):758–64.

[70] Hemberg O, Otendal M, Hertz HM. Liquid-metal-jet anode electron-impact X-ray source. Appl Phys Lett 2003;83:1483.

[71] Otendal M, Tuohimaa T, Hertz HM. Stability and debris in high-brightness liquid-metal-jet-anode microfocus X-ray sources. J Appl Phys 2007;101:026102.

[72] Otendal M et al. A 9 keV electron-impact liquid-gallium-jet X-ray source. Rev Sci Instrum 2008;79:016102.

[73] Carroll FE et al. Pulsed tunable monochromatic X-ray beams from a compact source. New opportunities. Am J Roentgenol 2003;181(5):1197–202.

[74] Kuroda R et al. Quasi-monochromatic hard X-ray source via laser Compton scattering and its application. Nucl Instrum Methods Phys Res Sect A: Accelerators, Spectrometers, Detectors and Associated Equipment; 2010.

[75] Urakawa J. Development of a compact X-ray source based on Compton scattering using a 1.3 GHz superconducting RF accelerating linac and a new laser storage cavity. Nucl Instrum Methods Phys Res Sect A 2010;637(1):S47–50.

[76] Yamada H. Novel X-ray source based on a tabletop synchrotron and its unique features. Nucl Instrum Methods Phys Res Sect B – Beam Interactions Mater. Atoms 2003;199:509–16.

[77] Toth R et al. Evaluation of ultrafast laser-based hard X-ray sources for phase-contrast imaging. Phys Plasmas 2007;14(5).

[78] Ketcham RA, Iturrino GJ. Nondestructive high-resolution visualization and measurement of anisotropic effective porosity in complex lithologies using high-resolution X-ray computed tomography. J Hydrol 2005;302(1–4):92–106.

[79] Latham S, Varslot T, Sheppard A. Image registration: enhancing and calibrating X-ray micro-CT imaging. In: International symposium of the society of core analysts, The Society of Core Analysts, Abu Dhabi, UAE; 2008.

[80] Bay BK et al. Digital volume correlation: three-dimensional strain mapping using X-ray tomography. Exp Mech 1999;39(3):217–26.

[81] Silin D et al. Microtomography and pore-scale modeling of two-phase fluid distribution. Transp Porous Media 2011;86(2):495–515.

[82] Iglauer S et al. Residual CO2 imaged with X-ray micro-tomography. Geophys Res Lett 2011;38(L21403):25.

[83] Coléou C et al. Three-dimensional snow images by X-ray microtomography. Ann Glaciol 2001;32(1):75–81.

[84] Flin F et al. Adaptive estimation of normals and surface area for discrete 3-D objects: application to snow binary data from X-ray tomography. IEEE Trans Image Process 2005;14(5):585–96.

[85] Flin F et al. Three-dimensional geometric measurements of snow microstructural evolution under isothermal conditions. In: Fohn, P.M.B., editor. Annals of glaciology, vol. 38; 2004. p. 39–44.

[86] Pieritz RA et al. From snow X-ray microtomograph raw volume data to micromechanics modeling: first results. In: Fohn PMB, editor. Annals of glaciology, vol. 38; 2004. p. 52–8.

[87] Kaempfer TU, Schneebeli M. Observation of isothermal metamorphism of new snow and interpretation as a sintering process. J Geophys Res – Atmos 2007;112(D24).

[88] Kaempfer TU, Schneebeli M, Sokratov SA. A microstructural approach to model heat transfer in snow. Geophys Res Lett 2005;32(21).

[89] Schneebeli M, Sokratov SA. Tomography of temperature gradient metamorphism of snow and associated changes in heat conductivity. Hydrol Process 2004;18(18):3655–65.

[90] Heggli M et al. Measuring snow in 3-D using X-ray tomography: assessment of visualization techniques. Ann Glaciol 2011;52(58):231–6.

[91] Culligan KA et al. Interfacial area measurements for unsaturated flow through a porous medium. Water Resour Res 2004;40(12).

[92] Porter ML et al. Measurement and prediction of the relationship between capillary pressure, saturation, and interfacial area in a NAPL–water–glass bead system. Water Resour Res 2010;46:1.

[93] Olsen PA et al. Characterizing solute transport in undisturbed soil cores using electrical and X-ray tomographic methods. Hydrol Process 1999;13(2):211–21.

[94] Han M et al. Deviation from Archie's law in partially saturated porous media: Wetting film versus disconnectedness of the conducting phase. Phys Rev E 2009;79(3).

[95] Kumar M et al. Probing the archie's exponent under variable saturation conditions. Petrophysics 2011;52(2):124–34.

[96] Watson HC, Roberts JJ. Connectivity of core forming melts: experimental constraints from electrical conductivity and X-ray tomography. Phys Earth Planet Inter 2011;186(3–4):172–82.

[97] Redwan M, Rammlmair D. Simultaneous monitoring of water saturation and fluid conductivity in unconsolidated sand columns. Soil Sci Soc Am J 2010;74(5):1457–68.

[98] Bay BK. Experimental measurement of three-dimensional continuum-level strain fields in trabecular bone. In: Majumdar SBBK, editor. Noninvasive assessment of trabecular bone architecture and the competence of bone; 2001. p. 181–97.

[99] Peth S et al. Non-invasive 3D analysis of local soil deformation under mechanical and hydraulic stresses by mu CT and digital image correlation. Soil Tillage Res 2010;111(1):3–18.

[100] Renard A et al. 3D imaging of fracture propagation using synchrotron X-ray microtomography. Earth Planet Sci Lett 2009;286(1–2):285–91.

[101] Gates M, Lambros J, Heath MT. Towards high performance digital volume correlation. Exp Mech 2011;51(4):491–507.

[102] Monsen K, Johnstad SE. Improved understanding of velocity–saturation relationships using 4D computer-tomography acoustic measurements. Geophys Prospect 2005;53(2):173–81.

[103] Louis L et al. Imaging strain localization by X-ray computed tomography: discrete compaction bands in Diemelstadt sandstone. J Struct Geol 2006;28(5):762–75.

[104] Charalampidou E-M et al. Characterization of shear and compaction bands in a porous sandstone deformed under triaxial compression. Tectonophysics 2011;503(1–2):8–17.

[105] Raynaud S et al. Experimental study of the relation between the permeability of kaolinite and its deformation at micro and macro scale. Int J Rock Mech Min Sci 2010;47(4):559–67.

[106] David C, Menendez B, Mengus JM. Influence of mechanical damage on fluid flow patterns investigated using CT scanning imaging and acoustic emissions techniques. Geophys Res Lett 2008;35(16).

[107] David C, Menendez B, Mengus JM. X-ray imaging of water motion during capillary imbibition: geometry and kinetics of water front in intact and damaged porous rocks. J Geophys Res – Solid Earth 2011;116.

[108] Wang Y et al. In situ high-pressure and high-temperature X-ray microtomographic imaging during large deformation: a new technique for studying mechanical behavior of multiphase composites. Geosphere 2011;7(1):40–53.

[109] Di Michiel M et al. Fast microtomography using high energy synchrotron radiation. Rev Sci Instrum 2005;76(4).

[110] Uesugi K, Sera T, Yagi N. Fast tomography using quasi-monochromatic undulator radiation. J Synchrotron Radiat 2006;13(5):403–7.

[111] Takano H et al. Fast X-ray micro-CT for real-time 4D observation. J Phys Conf Ser 2009;186:012049.

[112] Rack A et al. On the possibilities of hard X-ray imaging with high spatio-temporal resolution using polychromatic synchrotron radiation. J X-ray Sci Technol 2010;18(4):429–41.

[113] Mokso R et al. Real Time Tomography at the Swiss Light, Source, Melbourne (Australia); 2010.

[114] Grader AS et al. Computations of porosity and permeability of sparic carbonate using multi-scale CT images. In: Proceedings of the international symposium of the society of core analysts, SCA2009-31; 2009.

[115] Otsu N. Threshold selection method from gray-level histograms. IEEE Trans Syst Man Cybernet 1979;9(1):62–6.

[116] Ridler TW, Calvard S. Picture thresholding using an iterative selection method. IEEE Trans Syst Man Cybernet 1978;8(8):630–2.

[117] Iassonov P, Gebrenegus T, Tuller M. Segmentation of X-ray computed tomography images of porous materials: a crucial step for characterization and quantitative analysis of pore structures. Water Resour Res 2009;45.

[118] Porter ML, Wildenschild D. Image analysis algorithms for estimating porous media multiphase flow variables from computed microtomography data: a validation study. Comput Geosci 2010;14(1):15–30.

[119] Kivanc Mihcak M et al. Low-complexity image denoising based on statistical modeling of wavelet coefficients. IEEE Signal Process Lett 1999;6(12):300–3.

[120] Perona P, Malik J. Scale-space and edge-detection using anisotropic diffusion. IEEE Trans Pattern Anal Mach Intell 1990;12(7):629–39.

[121] Besag J. On the statistical analysis of dirty pictures. J Roy Statist Soc Ser B – Methodol 1986;48(3):259–302.

[122] Awate SP, Whitaker RT. Unsupervised, information-theoretic, adaptive image filtering for image restoration. IEEE Trans Pattern Anal Mach Intell 2006;28(3):364–76.

[123] Oh W, Lindquist WB. Image thresholding by indicator kriging. IEEE Trans Pattern Anal Mach Intell 1999;21(7):590–602.

[124] Wang W et al. Comparison of image segmentation methods in simulated 2D and 3D microtomographic images of soil aggregates. Geoderma 2011;162(3–4):231–41.

[125] Prodanovic M, Lindquist W, Seright R. 3D image-based characterization of fluid displacement in a Berea core. Adv Water Resour 2007;30(2):214–26.

[126] Geman S, Geman D. Stochastic relaxation, Gibbs distributions and the Bayesian restoration of images. IEEE Trans Pattern Anal Mach Intell 1984;6(6):721–41.

[127] Shi JB, Malik J. Normalized cuts and image segmentation. IEEE Trans Pattern Anal Mach Intell 2000;22(8):888–905.

[128] Boykov Y, Veksler O, Zabih R. Fast approximate energy minimization via graph cuts. IEEE Trans Pattern Anal Mach Intell 2001;23(11):1222–39.

[129] Zhu SC, Yuille A. Region competition: unifying snakes, region growing, and Bayes/MDL for multiband image segmentation. IEEE Trans Pattern Anal Mach Intell 1996;18(9):884–900.

[130] Kim JM et al. A nonparametric statistical method for image segmentation using information theory and curve evolution. IEEE Trans Image Process 2005;14(10):1486–502.

[131] Zhang YY, Brady M, Smith S. Segmentation of brain MR images through a hidden Markov random field model and the expectation-maximization algorithm. IEEE Trans Med Imaging 2001;20(1):45–57.

[132] Awate SP et al. Adaptive Markov modeling for mutual-information-based, unsupervised MRI brain-tissue classification. Med Image Anal 2006;10(5):726–39.

[133] Tohka J, Zijdenbos A, Evans A. Fast and robust parameter estimation for statistical partial volume models in brain MRI. Neuroimage 2004;23(1):84–97.

[134] Van Leemput K et al. A unifying framework for partial volume segmentation of brain MR images. IEEE Trans Med Imaging 2003;22(1):105–19.

[135] Hwang SN, Wehrli FW. Subvoxel processing: a method for reducing partial volume blurring with application to in vivo MR images of trablecular bone. Magn Reson Med 2002;47(5):948–57.

[136] Ayasso H, Mohammad-Djafari A. Joint NDT image restoration and segmentation using gauss-markov-potts prior models and variational bayesian computation. IEEE Trans Image Process 2010;19(9):2265–77.

[137] Mohebi A, Fieguth P, Ioannidis MA. Statistical fusion of two-scale images of porous media. Adv Water Resour 2009;32(11):1567–79.

[138] Ketcham RA, Slottke DT, Sharp Jr JM. Three-dimensional measurement of fractures in heterogeneous materials using high-resolution X-ray computed tomography. Geosphere 2010;6(5):499–514.

[139] Smith SM. Fast robust automated brain extraction. Hum Brain Mapp 2002;17(3):143–55.

[140] Myers GR et al. Phase-contrast tomography of single-material objects from few projections. Opt Exp 2008;16(2):908–19.

[141] Batenburg KJ. A network flow algorithm for binary image reconstruction from few projections. In: Discrete Geometry for Computer Imagery, Proceedings, Kuba ANLGPK, editor; 2006. p. 86–97.

[142] Leavers VF, Boyce JF. The Radon transform and its application to shape parametrization in machine vision. Image Vis Comput 1987;5(2):161–6.

[143] Duda RO, Hart PE. Use of the Hough transformation to detect lines and curves in pictures. Commun ACM 1972;15(1):11–5.

[144] Torquato S. Statistical description of microstructures. Annu Rev Mater Res 2002;32:77–111.

[145] Krause M et al. Determination of the fibre orientation in composites using the structure tensor and local X-ray transform. J Mater Sci 2010;45(4):888–96.

[146] Santalo LA. Integral geometry and geometric probability. Longman Higher Education; 1977.

[147] Mecke KR, Wagner H. Euler characteristic and related measures for random geometric sets. J Stat Phys 1991;64(3–4):843–50.

[148] Mecke KR, Buchert T, Wagner H. Robust morphological measures for large-scale structure in the universe. Astron Astrophys 1994;288(3):697–704.

[149] Schladitz K. Quantitative micro-CT. J Microsc 2011;243(2):111–7.

[150] Lehmann P et al. Tomographical imaging and mathematical description of porous media used for the prediction of fluid distribution. Vadose Zone J 2006;5(1):80.

[151] Vogel HJ, Weller U, Schluter S. Quantification of soil structure based on Minkowski functions. Comput Geosci 2010;36(10):1236–45.

[152] Schroder-Turk GE et al. Minkowski tensor shape analysis of cellular, granular and porous structures. Adv Mater 2011;23(22–23):2535–53.

[153] Kong TY, Rosenfeld A. Digital topology: introduction and survey. Comput Vision Graphics Image Process 1989;48(3):357–93.

[154] Edelsbrunner H, Letscher D, Zomorodian A. Topological persistence and simplification. Discrete Comput Geom 2002;28(4):511–33.

[155] Robins V, Wood PJ, Sheppard AP. Theory and algorithms for constructing discrete morse complexes from grayscale digital images. IEEE Trans Pattern Anal Mach Intell 2011;33(8):1646–58.

[156] Gyulassy A et al. A practical approach to morse-smale complex computation: scalability and generality. IEEE Trans Visual Comput Graphics 2008;14(6):1619–26.

[157] Glantz R, Hilpert M. Dual models of pore spaces. Adv Water Resour 2007;30(2):227–48.

[158] Glantz R, Hilpert M. Tight dual models of pore spaces. Adv Water Resour. 2008;31(5):787–806.

[159] Serra J. Image analysis and mathematical morphology. Academic Press; 1984.

[160] Hazlett RD. Simulation of capillary-dominated displacements in microtomographic images of reservoir rocks. Transp Porous Media 1995;20(1–2):21–35.

[161] Hilpert M, Miller CT. Pore-morphology-based simulation of drainage in totally wetting porous media. Adv Water Resour 2001;24(3–4):243–55.

[162] Arns CH, Knackstedt MA, Martys NS. Cross-property correlations and permeability estimation in sandstone. Phys Rev E 2005;72(4).

[163] Harrigan TP, Mann RW. Characterization of microstructural anisotropy in orthotropic materials using a 2nd rank tensor. J Mater Sci 1984;19(3):761–7.

[164] Odgaard A et al. Fabric and elastic principal directions of cancellous bone are closely related. J Biomech 1997;30(5):487–95.

[165] Ketcham RA. Three-dimensional grain fabric measurements using high-resolution X-ray computed tomography. J Struct Geol 2005;27(7):1217–28.

[166] Saha PK, Gomberg BR, Wehrli FW. Three-dimensional digital topological characterization of cancellous bone architecture. Int J Imaging Syst Technol 2000;11(1):81–90.

[167] Iglauer S et al. X-ray tomography measurements of power-law cluster size distributions for the nonwetting phase in sandstones. Phys Rev E 2010;82(5).

[168] Liu J, Regenauer-Lieb K. Application of percolation theory to microtomography of structured media: percolation threshold, critical exponents, and upscaling. Phys Rev E 2011;83(1).

[169] Denison C, Carlson WD, Ketcham RA. Three-dimensional quantitative textural analysis of metamorphic rocks using high-resolution computed X-ray tomography. 1: Methods and techniques. J Metamorph Geol 1997;15(1):29–44.

[170] Beucher S, Lantuejoul C. Use of watersheds in contour detection. In: International workshop on image processing: real-time edge and motion detection/estimation, Rennes, France; 1979.

[171] Ketcham RA. Computational methods for quantitative analysis of three-dimensional features in geological specimens. Geosphere 2005;1(1):32–41.

[172] Thompson KE et al. Application of a new grain-based reconstruction algorithm to microtomography images for quantitative characterization and flow modeling. SPE J 2008;13(2):164–76.

[173] Sheppard AP et al. Analysis of rock microstructure using high-resolution X-ray tomography. In: 2006 international symposium of the society of core analysts. Trondheim, Norway: Society of Core Analysts; 2006.

[174] Claussen JC. Offdiagonal complexity: a computationally quick complexity measure for graphs and networks. Phys A – Statist Mech Appl 2007;375(1):365–73.

[175] Shakarji CM. Least-squares fitting algorithms of the NIST algorithm testing system. J Res Nat Inst Stand Technol 1998;103(6):633–41.

[176] Krumbein WC, Sloss LL. Stratigraphy and sedimentation. San Francisco: W.H. Freeman; 1963.

[177] Garboczi EJ. Three-dimensional mathematical analysis of particle shape using X-ray tomography and spherical harmonics: application to aggregates used in concrete. Cem Concr Res 2002;32(10):1621–38.

[178] Erdogan ST et al. Three-dimensional shape analysis of coarse aggregates: new techniques for and preliminary results on several different coarse aggregates and reference rocks. Cem Concr Res 2006;36(9):1619–27.

[179] Taylor MA et al. Some properties of irregular 3-D particles. Powder Technol 2006;162(1):1–15.

[180] Erdogan ST et al. Micrometer-scale 3-D shape characterization of eight cements: Particle shape and cement chemistry, and the effect of particle shape on laser diffraction particle size measurement. Cem Concr Res 2010;40(5):731–9.

[181] Lindquist WB et al. Medial axis analysis of void structure in three-dimensional tomographic images of porous media. J Geophys Res 1996;101(B4):8297–310.

[182] Lindquist WB et al. Pore and throat size distributions measured from synchrotron X-ray tomographic images of Fontainebleau sandstones. J Geophys Res 2000;105(B9):21509–27.

[183] Vogel HJ, Roth K. Quantitative morphology and network representation of soil pore structure. Adv Water Resour 2001;24(3–4):233–42.

[184] Al-Raoush RI, Willson CS. Extraction of physically realistic pore network properties from three-dimensional synchrotron X-ray microtomography images of unconsolidated porous media systems. J Hydrol 2005;300(1–4):44–64.

[185] Sheppard AP, Sok RM, Averdunk H. Improved pore network extraction methods. In: International symposium of the society of core analyst. Toronto, Canada: Society of Core Analysts; 2005.

[186] Al-Kharusi AS, Blunt MJ. Network extraction from sandstone and carbonate pore space images. J Petrol Sci Eng 2007;56(4):219–31.

[187] Jiang Z et al. Efficient extraction of networks from three-dimensional porous media. Water Resour Res 2007;43(12).

[188] Peth S et al. Three-dimensional quantification of intra-aggregate pore-space features using synchrotron-radiation-based microtomography. Soil Sci Soc Am J 2008;72(4):897.

[189] Lindquist WB, Venkatarangan A. Investigating 3D geometry of porous media from high resolution images. Phys Chem Earth Part A 1999;24(7):593–9.

[190] Prodanović M, Lindquist WB, Seright RS. Porous structure and fluid partitioning in polyethylene cores from 3D X-ray microtomographic imaging. J Colloid Interface Sci 2006;298(1):282–97.

[191] Lorensen WE, Cline HE. Marching cubes: a high resolution 3D surface construction algorithm. Comput Graphics 1987;21(4).

[192] Ruppert J. A Delaunay refinement algorithm for quality 2-dimensional mesh generation. J Algor 1995;18(3):548–85.

[193] Shewchuk JR. Delaunay refinement algorithms for triangular mesh generation. Comput Geom – Theory Appl 2002;22(1–3):21–74.

[194] Dalla E, Hilpert M, Miller CT. Computation of the interfacial area for two-fluid porous medium systems. J Contam Hydrol 2002;56(1–2):25–48.

[195] McClure JE et al. Approximation of interfacial properties in multiphase porous medium systems. Adv Water Resour 2007;30(3):354–65.

[196] Rodriguez E, Prodanovic M, Bryant SL. Contact line extraction and length measurements in model sediments and sedimentary rocks. J Colloid Interface Sci 2011;368(1):558–77.

[197] Flynn PJ, Jain AK. On reliable curvature estimation. In: Computer vision and pattern recognition. San Diego, CA, USA: IEEE Computer Society; 1989.

[198] Taubin G. Estimating the tensor of curvature of a surface from a polyhedral approximation. In: Fifth international conference on computer vision, proceedings; 1995. p. 902–7.

[199] Magid E, Soldea O, Rivlin E. A comparison of Gaussian and mean curvature estimation methods on triangular meshes of range image data. Comput Vis Image Understand 2007;107(3):139–59.

[200] Meyer N et al. Discrete differential-geometry operators for triangulated 2-manifolds. Visualiz Math III 2003:35–57.

[201] Rusinkiewicz S. Estimating curvatures and their derivatives on triangle meshes. In: IEEE Proceedings, 2nd international symposium on 3D data processing, visualization and transmission, 3DPVT 2004; 2004. p. 486–93.

[202] Chopp DL, Sethian JA. Flow under curvature: singularity formation, minimal surfaces, and geodesics. Exp Math 1993;2(4):235–55.

[203] Flin F, et al. Full three-dimensional modelling of curvature-dependent snow metamorphism: first results and comparison with experimental tomographic data, J Phys D – Appl Phys 2003;36(10A):A49–54.

[204] Blunt MJ. Flow in porous media – pore-network models and multiphase flow. Curr Opin Colloid Interface Sci 2001;6(3):197–207.

[205] Auzerais FM et al. Transport in sandstone: a study based on three dimensional microtomography. Geophys Res Lett 1996;23(7):705–8.

[206] Shan X, Chen H. Lattice-Boltzmann model for simulating flows with interparticle interaction. Phys Rev E 1993;47:1815–9.

[207] Gunstensen AK et al. Lattice Boltzmann model of immiscible fluids. Phys Rev A 1991;43(8):4320–7.

[208] Tolke J et al. Lattice Boltzmann simulations of binary fluid flow through porous media. Philos Trans Roy Soc London Ser A – Math Phys Eng Sci 2002;360(1792):535–45.

[209] Prodanovic M, Bryant SL. A level set method for determining critical curvatures for drainage and imbibition. J Colloid Interface Sci 2006;304(2):442–58.

[210] Vogel HJ et al. Comparison of a Lattice-Boltzmann model, a full-morphology model, and a pore network model for determining capillary pressure–saturation relationships. Vadose Zone J 2005;4(2):380–8.

[211] Ahrenholz B et al. Prediction of capillary hysteresis in a porous material using lattice-Boltzmann methods and comparison to experimental data and a morphological pore network model. Adv Water Resour 2008;31(9):1151–73.

[212] Vogel HJ. Morphological determination of pore connectivity as a function of pore size using serial sections. Eur J Soil Sci 1997;48(3):365–77.

[213] Baldwin CA et al. Determination and characterization of the structure of a pore space from 3D volume images. J Colloid Interface Sci 1996;181(1):79–92.

[214] Silin DB, Jin GD, Patzek TW. Robust determination of the pore-space morphology in sedimentary rocks. J Petrol Technol 2004;56(5):69–70.

[215] Youssef S, et al. Quantitative 3D characterisation of the pore space of real rocks: improved μCT resolution and pore extraction methodology. In: International symposium of the society of core analysts; 2007. p. SCA2007-17.

[216] Liang Z, Ioannidis MA, Chatzis I. Geometric and topological analysis of three-dimensional porous media: pore space partitioning based on morphological skeletonization. J Colloid Interface Sci 2000;221(1):13–24.

[217] Silin D, Patzek T. Pore space morphology analysis using maximal inscribed spheres. Phys A: Statist Theor Phys 2006;371(2):336–60.

[218] Dong H, Blunt MJ. Pore-network extraction from micro-computerized-tomography images. Phys Rev E 2009;80(3):56.

[219] Monga O et al. 3D geometric structures and biological activity: application to microbial soil organic matter decomposition in pore space. Ecol Model 2008;216(3–4):291–302.

[220] Ngom NF et al. Extraction of three-dimensional soil pore space from microtomography images using a geometrical approach. Geoderma 2011;163(1–2):127–34.

[221] Al-Raoush R, Thompson K, Willson CS. Comparison of network generation techniques for unconsolidated porous media. Soil Sci Soc Am J 2003;67(6):1687–700.

[222] Dong H et al. Pore network modelling on carbonate: a comparative study of different Micro-CT network extraction methods. In: International symposium of the society of core analysts, Society of Core Analysts; 2008.

[223] Oren PE, Bakke S, Arntzen OJ. Extending predictive capabilities to network models. SPE J 1998;3(4):324–36.

[224] Arns JY et al. Pore-level validation of representative pore networks obtained from micro-ct images. In: The International Symposium of the Society of Core Analysts, Calgary, Canada; 2007.

[225] Sholokhova Y, Kim D, Lindquist WB. Network flow modeling via lattice-Boltzmann based channel conductance. Adv Water Resour 2009;32(2):205–12.

[226] Patzek TW, Silin DB. Shape factor and hydraulic conductance in noncircular capillaries I. One-phase creeping flow. J Colloid Interface Sci 2001;236(2):295–304.

[227] Lindquist WB. The geometry of primary drainage. J Colloid Interface Sci 2006;296(2):655–68.

[228] Promentilla MAB, Sugiyama T. X-ray microtomography of mortars exposed to freezing-thawing action. J Adv Concrete Technol 2010;8(2):97–111.

[229] Petrovic AM, Siebert JE, Rieke PE. Soil bulk-density analysis in 3 dimensions by computed tomographic scanning. Soil Sci Soc Am J 1982;46(3):445–50.

[230] Hainsworth J, Aylmore L. The use of computer assisted tomography to determine spatial distribution of soil water content. Aust J Soil Res 1983;21(4):435.

[231] Crestana S, Mascarenhas S, Pozzi-Mucelli RS. Static and dynamic three-dimensional studies of water in soil using computed tomographic scanning. Soil Sci 1985;140(5):326–32.

[232] Anderson SH et al. Rapid nondestructive bulk-density and soil-water content determination by computed tomography. Soil Sci Soc Am J 1988;52(1):35–40.

[233] Wang SY et al. Reconstruction of oil saturation distribution histories during immiscible liquid–liquid displacement by computer-assisted tomography. AIChE J 1984;30(4):642–6.

[234] Wellington SL, Vinegar HJ. X-ray computerized tomography. J Petrol Technol 1987;39(8).

[235] Hunt PK, Engler P, Bajsarowicz C. Computed-tomography as a core analysis tool – applications, instrument evaluation, and image improvement techniques. J Petrol Technol 1988;40(9):1203–10.

[236] Vinegar HJ, Wellington SL. Tomographic imaging of three-phase flow experiments. Rev Sci Instrum 1987;58(1):96.

[237] Withjack EM. Computed tomography for rock-property determination and fluid-flow visualization. SPE Format Evaluat 1988;3(4):696–704.

[238] Jasti JK, Jesion G, Feldkamp L. Microscopic imaging of porous-media with X-ray computer-tomography. SPE Format Evaluat 1993;8(3):189–93.

[239] Clausnitzer V, Hopmans JW. Pore-scale measurements of solute breakthrough using microfocus X-ray computed tomography. Water Resour Res 2000;36(8):2067.

[240] Spanne P et al. Synchrotron computed microtomography of porous media: topology and transports. Phys Rev Lett 1994;73(14):2001–4.

[241] Coker DA, Torquato S, Dunsmuir JH. Morphology and physical properties of Fontainebleau sandstone via a tomographic analysis. J Geophys Res 1996;101(B8):17497–506.

[242] Coles ME et al. Pore level imaging of fluid transport using synchrotron X-ray microtomography. J Petrol Sci Eng 1998;19(1–2):55–63.

[243] Werth CJ et al. A review of non-invasive imaging methods and applications in contaminant hydrogeology research. J Contam Hydrol 2010;113(1–4):1–24.

[244] Taina IA, Heck RJ, Elliot TR. Application of X-ray computed tomography to soil science. A literature review. Can J Soil Sci 2008;88(1):1–20.

[245] Seright R. Use of X-ray computed microtomography to understand why gels reduce relative permeability to water more than that to oil. J Petrol Sci Eng 2003;39(3–4):217–30.

[246] Turner M. Three-dimensional imaging of multiphase flow in porous media. Physica A 2004;339(1–2):166–72.

[247] Wildenschild D et al. Quantitative analysis of flow processes in a sand using synchrotron-based X-ray microtomography. Vadose Zone J 2005;4(1):112–26.

[248] Al-Raoush R, Willson C. A pore-scale investigation of a multiphase porous media syste. J Contam Hydrol 2005;77(1–2):67–89.

[249] Schnaar G, Brusseau ML. Pore-scale characterization of organic immiscible-liquid morphology in natural porous media using synchrotron X-ray microtomography. Environ Sci Technol 2005;39(21):8403–10.

[250] Culligan KA et al. Pore-scale characteristics of multiphase flow in porous media: a comparison of air–water and oil–water experiments. Adv Water Resour 2006;29(2):227–38.

[251] Schaap MG et al. Comparison of pressure-saturation characteristics derived from computed tomography and lattice Boltzmann simulations. Water Res Res 43(12) (2007).

[252] Porter ML, Schaap MG, Wildenschild D. Lattice-Boltzmann simulations of the capillary pressure-saturation-interfacial area relationship for porous media. Adv Water Resour 2009;32(11):1632–40.

[253] Youssef S et al. Towards a better understanding of multiphase flow in porous media: 3D in-situ fluid distribution imaging at the pore scale. In: International symposium of the society of core analysts held in Noordwijk, The Netherlands 27–30 September, 2009, SCA2009-17; 2009.

[254] Karpyn ZT, Piri M, Singh G. Experimental investigation of trapped oil clusters in a water-wet bead pack using X-ray microtomography. Water Resour Res 2010;46(4).

[255] Schnaar G, Brusseau ML. Characterizing pore-scale dissolution of organic immiscible liquid in natural porous media using synchrotron X-ray microtomography. Environ Sci Technol 2006;40(21):6622–9.

[256] Al-Raoush RI. Impact of wettability on pore-scale characteristics of residual nonaqueous phase liquids. Environ Sci Technol 2009;43(13):4796–801.

[257] Kumar M et al. Visualizing and quantifying the residual phase distribution in core material. Noordwijk; The Netherlands: Society of Core Analysts; 2009.

[258] Singh K et al. Remobilization of residual non-aqueous phase liquid in porous media by freeze−thaw cycles. Environ Sci Technol 2011;45(8):3473–8.

[259] Armstrong RT, Wildenschild D. Microbial enhanced oil recovery in fractional-wet systems: a pore-scale investigation. Transp Porous Media 2012. http://dx.doi.org/10.1007/s11242-011-9934-3.

[260] Reeves PC, Celia MA. A functional relationship between capillary pressure, saturation, and interfacial area as revealed by a pore-scale network model. Water Resour Res 1996;32(8):2345–58.

[261] Berkowitz B, Hansen DP. A numerical study of the distribution of water in partially saturated porous rock. Transp Porous Media 2001;45(2):303–19.

[262] Hassanizadeh SM, Gray WG. Thermodynamic basis of capillary pressure in porous media. Water Resour Res 1993;29(10):3389.

[263] Gray W, Hassanizadeh S. Unsaturated flow theory including interfacial phenomena. Water Resour Res 1991;27(8):1855–63.

[264] Brusseau ML et al. Synchrotron X-ray microtomography and interfacial partitioning tracer test measurements of NAPL-water interfacial areas. Water Resour Res 2008;44(1).

[265] Brusseau ML et al. Relationships among air-water interfacial area, capillary pressure, and water saturation for a sandy porous medium. Water Resour Res 2006;42(3).

[266] Brusseau ML et al. Measuring air−water interfacial areas with X-ray microtomography and interfacial partitioning tracer tests. Environ Sci Technol 2007;41(6):1956–61.

[267] Narter M, Brusseau ML. Comparison of interfacial partitioning tracer test and high-resolution microtomography measurements of fluid–fluid interfacial areas for an ideal porous medium. Water Resour Res 2010;46(8).

[268] Schnaar G, Brusseau ML. Characterizing pore-scale configuration of organic immiscible liquid in multiphase systems with synchrotron X-ray microtomography. Vadose Zone J 2006;5(2):641.

[269] Costanza-Robinson MS, Harrold KH, Lieb-Lappen RM. X-ray microtomography determination of air−water interfacial area−water saturation relationships in sandy porous media. Environ Sci Technol 2008;42(8):2949–56.

[270] Costanza-Robinson MS, Estabrook BD, Fouhey DF. Representative elementary volume estimation for porosity, moisture saturation, and air–water interfacial areas in unsaturated porous media: data quality implications. Water Resour Res 2011;47(7).

[271] Han J, Jin Y, Willson CS. Virus retention and transport in chemically heterogeneous porous media under saturated and unsaturated flow conditions. Environ Sci Technol 2006;40(5):1547–55.

[272] Kumar M, et al. Imaging of pore scale distribution of fluids and wettability. In: International symposium of the society of core analysts, SCA2008-16; 2008.

[273] Landry CJ, Karpyn ZT, Piri M. Pore-scale analysis of trapped immiscible fluid structures and fluid interfacial areas in oil-wet and water-wet bead packs. Geofluids 2011;11(2):209–27.

[274] Carminati A et al. Unsaturated water flow across soil aggregate contacts. Adv Water Resour 2008;31(9):1221–32.

[275] Kaestner A, Lehmann E, Stampanoni M. Imaging and image processing in porous media research. Adv Water Resour 2008;31(9):1174–87.

[276] Tippkötter R et al. Detection of soil water in macropores of undisturbed soil using microfocus X-ray tube computerized tomography (μCT). Soil Tillage Res 2009;105(1):12–20.

[277] Alvarado FE et al. Visualization of the three phases in porous media using micro computed tomography. In: Proceedings of the 2003 international symposium of the society of core analysts meeting, Pau, France, SCA2003-21; 2003.

[278] Brown KI et al. Interfacial area measurements for robust models of multiphase flow in porous media.In International Goldschmidt conference, August 14–19, 2011 in Prague, Czech Republic; 2011.

[279] Nunan N et al. Investigating microbial micro-habitat structure using X-ray computed tomography. Geoderma 2006;133(3–4):398–407.

[280] Thieme J. X-ray tomography of a microhabitat of bacteria and other soil colloids with sub-100 nm resolution. Micron 2003;34(6–7):339–44.

[281] Altman S, Peplinski W, Rivers M. Evaluation of synchrotron X-ray computerized microtomography for the visualization of transport processes in low-porosity materials. J Contam Hydrol 2005;78(3):167–83.

[282] Cai R et al. Tomographic analysis of reactive flow induced pore structure changes in column experiments. Adv Water Resour 2009;32(9):1396–403.

[283] Noiriel C et al. Hydraulic properties and microgeometry evolution accompanying limestone dissolution by acidic water. Oil Gas Sci Technol 2005;60(1):177–92.

[284] Noiriel C et al. Changes in reactive surface area during limestone dissolution: an experimental and modelling study. Chem Geol 2009;265(1–2):160–70.

[285] Luquot L, Gouze P. Experimental determination of porosity and permeability changes induced by injection of CO_2 into carbonate rocks. Chem Geol 2009;265:148–59.

[286] Flukiger F, Bernard D. A new numerical model for pore scale dissolution of calcite due to CO_2 saturated water flow in 3D realistic geometry: principles and first results. Chem Geol 2009;265(1–2):171–80.

[287] Gouze P, Luquot L. X-ray microtomography characterization of porosity, permeability and reactive surface changes during dissolution. J Contam Hydrol 2011;120(21-SI):45–55.

[288] Armstrong R, Ajo-Franklin J. Investigating biomineralization using synchrotron based X-ray computed microtomography. Geophys Res Lett 2011;38(L08406).

[289] Li X et al. Pore-scale observation of microsphere deposition at grain-to-grain contacts over assemblage-scale porous media domains using X-ray microtomography. Environ Sci Technol 2006;40(12):3762–8.

[290] Chen C, Packman AI, Gaillard JF. Using X-ray micro-tomography and pore-scale modeling to quantify sediment mixing and fluid flow in a developing streambed. Geophys Res Lett 2009; 36(8).

[291] Chen C et al. A multi-scale investigation of interfacial transport, pore fluid flow, and fine particle deposition in a sediment bed. Water Resour Res 2010;46(11).

[292] Hansel CM et al. Characterization of Fe plaque and associated metals on the roots of mine-waste impacted aquatic plants. Environ Sci Technol 2001;35(19):3863–8.

[293] Hansel CM et al. Spatial and temporal association of As and Fe species on aquatic plant roots. Environ Sci Technol 2002;36(9):1988–94.

[294] Keon NE et al. Combined XAS and chemical extraction investigation of arsenic distribution in sediment phases and in cattail roots. Abstracts of Papers of the American Chemical Society, 223: p. 127-GEOC; 2002.

[295] Blute NK et al. Arsenic sequestration by ferric iron plaque on cattail roots. Environ Sci Technol 2004;38(22):6074–7.

[296] Lombi E et al. Fast X-ray fluorescence microtomography of hydrated biological samples. PLoS ONE 2011;6(6).

[297] Katsevich A. Theoretically exact filtered backprojection-type inversion algorithm for spiral CT. SIAM J Appl Math 2002; 2012–2026.